

AN ABSTRACT OF THE THESIS OF

Chih-Heng Tseng for the degree of Master of Science in Industrial Manufacturing Engineering
presented on December 19, 2003

Title: The Impact of Fabrication Methods on the Mass Flux Characteristics of Contactor Membranes in
Absorption/Desorption Cycle Micro-Scale Heat Pumps

Abstract approved:

Redacted for privacy

Brian K. Paul

A key requirement within many microsystem devices is the ability for rapid mixing and gas-liquid absorption. In the past, qualitative results have suggested that micro-manufactured straight-through pores can significantly reduce the pressure drop for gas diffusion across a gas-liquid contactor as compared to the complicated and tortuous flow paths encountered in commercially available membranes. In this study, the mass transfer performance of several micromachined membranes are compared with the performance of conventional membranes. A tortuosity factor is introduced to serve as a standard for comparing the morphology of the different membranes. Two membranes with straight-through pores are micro-manufactured. The first approach involved the deep UV (266 nm) laser micromachining of 75 μm thick Kapton film. The second approach involved the micro-molding of thin polydimethylsiloxane (PDMS) membranes using soft lithography techniques. Pores as small as 5 μm were fabricated with both approaches. A novel technique for producing pores with 3:1 aspect-ratio in PDMS is introduced. Results show that woven membranes provide outstanding mass transfer performance. However, woven membranes are not very stiff and their complex morphology makes their potential for fluidic breakthrough difficult to assess. The laser-machined membranes were also found to give 10 to 30 times the mass flux of conventional membranes. The micro-molded PDMS membranes

were found to be unsuitable for mass transfer at pore sizes down to 5 μm due collapsing pores. Several alternatives are presented for improving the performance of micro-manufactured membranes.

©Copyright by Chih-Heng Tseng
December 19, 2003
All Rights Reserved

The Impact of Fabrication Methods on the Mass Flux Characteristics of Contactor Membranes in
Absorption/Desorption Cycle Micro-Scale Heat Pumps

by
Chih-Heng Tseng

A THESIS
submitted to
Oregon State University

In partial fulfillment of
the requirements for the
degree of

Master of Science

Presented December 19, 2003

Commencement June 2004

Master of Science thesis of Chih-Heng Tseng presented on December 19, 2003

APPROVED:

Redacted for privacy

Major Professor, representing Industrial Engineering

Redacted for privacy

Head of the Department of Industrial and Manufacturing Engineering

Redacted for privacy

Dean of the Graduate School

I understand that my thesis will become part of the permanent collection of Oregon State University libraries. My signature below authorizes release of my thesis to any reader upon request.

Redacted for privacy

Chih-Heng Tseng, Author

ACKNOWLEDGMENTS

I would like to thank Dr. Brian K. Paul for giving me an opportunity to work on the Heat Pump project which turned into my master thesis. The advice and support I got from him was very important to me. I learned not only the knowledge, but also the passion to pursue knowledge and to make the world of a difference. Many professors such as Dr. Drost, Dr. Pence, and Dr. Peterson...etc. all helped me a lot when I needed guidance.

One thing I enjoyed the most in OSU is the friends that I had for the last two years. They are all wonderful persons with great personalities despite the different nationality. I like to thank them for standing beside me and provide me the courage to continue my study.

I also would like to express my gratitude to my parents for providing me both mental and financial support throughout my study. My girlfriend, Sandy, was great for giving me the strength to carry on.

TABLE OF CONTENTS

	<u>Page</u>
CHAPTER 1 INTRODUCTION	1
CHAPTER 2 LITERATURE REVIEW	3
2.1 Measuring membrane tortuosity	3
2.2 Microfabrication of Low Tortuosity Membranes.....	6
2.3 Thesis Statement	6
CHAPTER 3 Engineered Membrane Design and Fabrication	8
3.1 Membrane design.....	8
3.2 Laser Micromachining Approach.....	9
3.3 Micromolded Approach	14
CHAPTER 4 EXPERIMENTAL APPROACH	20
4.1 Baseline Measurements.....	20
4.2 Experimental approach for laser micromachining and micromolded membrane.....	22
CHAPTER 5 RESULTS AND DISCUSSION	23
5.1 Mass Flux Results for Commercial Membranes.....	23
5.1.1 Baseline Results	23
5.1.2 Normalized Results for Non-Engineered Membranes	24
5.1.3 Normalized Results for Woven Membranes	27
5.2 Laser Micromachining Membrane Results	28
5.2.1 Laser Micromachined Membranes.....	28
5.2.2 Normalized Results for Laser Micromachined Membrane..	31
5.4 Permeability Versus Porosity, Thickness, and Pore Size	34
5.5 Discussion of Micromolded Membrane Results	39
CHAPTER 6 CONCLUSION.....	44
Bibliography	49
Appendices	51

Appendix H	70
H.1 SU8 Posts	70
H.2 PDMS	73
H.3 Sacrificial Layer	74

TABLE OF FIGURES

	<u>Page</u>
Figure 1: Gaussian beam properties	10
Figure 2: Hole patterns with 200 μm height variance	11
Figure 3: Hole patterns with 20 μm height variance	11
Figure 4: 3-D and 2-D view of laser profile at 18 amps.....	13
Figure 5: 3-D and 2-D view of laser profile at 17 amps.....	13
Figure 6: Structural formula of PDMS.....	14
Figure 7: Comparison between glass and silicon substrate. (Adhesion promoter was used in both instances)	16
Figure 8: Schematic of process steps for PDMS membrane fabrication.....	18
Figure 9: A simple schematic of the membrane mass flux test loop	20
Figure 10: Physical layout of the membrane mass flux test loop.....	21
Figure 11: Physical layout of the membrane mass flux test fixture.	21
Figure 12: Average pressure drop results as a function of mass flux across the baseline membranes.	23
Figure 13: Normalized pressure drop results as a function of normalized mass flux across the baseline membranes.	21
Figure 14: Normalized pressure drop results for networked, fibrous, and tortuous structures	26
Figure 15: Normalized pressure drop results for different pore size structures	26
Figure 16: Comparison of woven membrane with commercial membranes with similar pore size.	27

TABLE OF FIGURES (Continue)

	<u>Page</u>
Figure 17: Front side pore array with 100 μm spacing and average pore size of $16.5 \pm 0.5 \mu\text{m}$	28
Figure 18: Back side pore array with 100 μm spacing and average pore size of $5.3 \pm 0.8 \mu\text{m}$	29
Figure 19: Front side of the Polycarbonate pore with 200X	30
Figure 20: Back side of the Polycarbonate pore with 500X.....	30
Figure 21: Normalized mass flux results for the laser micromachined membranes compared with Figure 16.	32
Figure 22: SEM Pictures of Frontside and Backside of the pore	33
Figure 23: SEM pictures showing evidence of surface roughness just inside the backside pore exit.....	34
Figure 24: Tortuosity versus porosity plot. Membranes found in the lower, left quadrant would tend to have higher permeability with lower stiffness. ...	35
Figure 25: Tortuosity versus Thickness.....	36
Figure 26: Permeability versus Pore Size.....	37
Figure 27: Front side of PDMS membrane pore	39
Figure 28: Sealed PDMS pores before application of IPA	40
Figure 29: Portion of PDMS pores opened after few drops of IPA	40
Figure 30: All PDMS pores opened after full application of IPA.	40
Figure 31: AFM picture of a pore A	42
Figure 32: AFM picture of a pore B	42

LIST OF TABLES

	<u>PAGE</u>
Table 1: Experiment data	73
Table 2: PDMS experiments result	74

THE IMPACT OF FABRICATION METHODS ON THE MASS FLUX CHARACTERISTICS OF CONTACTOR MEMBRANES IN ABSORPTION/DESORPTION CYCLE MICRO-SCALE HEAT PUMPS

CHAPTER 1

INTRODUCTION

Recent developments at the Pacific Northwest National Laboratory and Oregon State University suggest that the performance of absorption and desorption systems can be significantly enhanced by the use of a thin film gas/liquid contactor. A contactor is a porous membrane that employs microtechnology-based structures to mechanically constrain the gas/liquid interface. This technology can be used to form very thin liquid films with a film thickness of less than 100 microns while still allowing gas/liquid contact (Davis, 1998; Drost, et al., 1999).

When the resistance to mass transfer in gas desorption and absorption is dominated by diffusion in the liquid phase, the use of thin contactors (<100 microns) for desorption and absorption can radically reduce the size of a gas desorber or absorber. The development of compact absorbers and desorbers enables the deployment of small heat-actuated absorption heat pumps for distributed space heating and cooling applications, heat-actuated automotive air conditioning, and manportable cooling (Champagne, et al., 2001). The contactors are also suitable for the development of high capacity CO₂ absorption devices for CO₂ collection and sequestration (Drost, et al., 1999; TeGrotenhuis, et al.).

One limiting factor on the development of heat-actuated absorption cycle heat pumps is the lack of driving pressure within the absorber. Generally, pressure drop across the contactor membrane must be minimized in order to maximize mass transfer rates.

Previous findings have suggested that micromanufactured straight-through pores can significantly reduce the pressure drop for gas diffusion across a contactor as compared to the complicated and tortuous flow paths encountered in commercially available membranes. The purpose of this study is to compare the mass transfer performance of conventional membranes with those having engineered pores, to quantify the benefit for heat pump contactors. A baseline for mass flux measurements is established by testing twenty-three different conventional membranes. To parse the enormous list of commercial membranes, selection criteria were set which indicated that the membranes were made from polymers with thicknesses between 50 and 150 μm and pore sizes from 1 to 10 μm . The morphology of each membrane is studied by micrograph and related to the tortuosity factor calculated from the mass flux measurements. Two sets of micromanufactured straight-through pore membranes are produced by laser micromaching and soft micromolding (McDonald, et al., 2002). Both are tested and compared to the baseline mass flux measurements.

CHAPTER 2

LITERATURE REVIEW

2.1 Measuring membrane tortuosity

Membrane technology is built on the knowledge of the performance of particular membranes under different external flow conditions. The better the membrane characteristics are understood and quantified, the better the chances are of success in new applications and systems (Plessis, 1992). For the contactor application in the heat pump, permeability (the mass transfer as a function of pressure difference across the membrane) is the dominant characteristic that needs to be quantified. Higher permeability shows the membrane has high mass transfer and low pressure difference. In previous studies, gas penetration tests have been utilized to quantify permeability (Iversen S.B., et al., 1997; Plessis, 1992; Shelekhin, et al., 1993).

The permeability L_p of a contactor membrane is defined by

$$L_p = \frac{\ddot{M}}{\Delta p} \quad (1)$$

where \ddot{M} is the mass flux and Δp is the pressure difference across the membrane.

The mass flux can be expressed as a function of volume flow through the membrane J_v

$$\ddot{M} = \frac{J_v \cdot \rho}{A} = \frac{J_v \cdot \rho}{\frac{\pi}{4} \cdot d_m} \quad (2)$$

where A is the nominal area of the membrane exposed to the fluid, ρ is the density of the fluid and d_m is

the diameter of the test fixture plenum.

Substituting equation (2) into equation (1), the permeability can be expressed as

$$L_p = \frac{J_v \cdot \rho}{\Delta p} \quad (3)$$

$$\therefore L_p = f(J_v)$$

In the membrane literature, the volume flow through the membrane J_v follows the well-established Hagen-Poiseuille relationship defined as

$$J_v = \frac{\Theta d_p^2}{32 \eta \psi} \left(\frac{\Delta p}{\Delta x} \right) \quad (4)$$

where Δp is the pressure difference, ψ is the mean tortuosity factor for all the pores, d_p is the equivalent or hydrodynamic pore diameter, Θ is the porosity (void volume per total volume), η is the absolute viscosity of the fluid (M/Lt*) and Δx is the membrane thickness (White, 1994). This equation has been found to apply to microporous membranes (W.S., et al., 1992; Marcel, 1990).

From Hagen-Poiseuille, $L_p = f(J_v) = f\left(\frac{1}{\psi}\right)$ for membranes which indicate that low tortuosity membranes are needed to maximize permeability. In the membrane literature, the tortuosity of a membrane is defined as the degree to which the pores in the membrane depart from uniform straight-through conditions. In particular, the tortuosity factor (ψ) for a membrane is a multiplier that takes into consideration the variation in the cross-sectional shape of pores in a membrane as well as the variation in angle between the pore axes and the mass flow direction (Salmas, et al., 2001; Saripalli, et al., 2002). To quantify the tortuosity of a membrane (commercial and engineered), the Hagen-Poiseuille equation is used (Marcel, 1990; Palacio, et al., 1999; W.S., et al., 1992).

* M/Lt = 1 kg/(m·s) = 0.0209 slug/(ft·s)

From equation (4), the tortuosity factor ψ can also be solved as

$$\psi = \frac{\left(\frac{\Delta p}{\Delta x} \right)}{\left(\frac{32\eta J_v}{\Theta d_p^2} \right)} \quad (5)$$

this suggests the slope of the plot of the numerator versus the denominator is an indicator of the tortuosity factor for the membrane. In order to quantify the tortuosity of a membrane, several quantities are needed. The absolute viscosity, η , is assumed to be constant. The variables $\dot{M} (= \eta J_v)$, ΔP and Θ are measured experimentally. The membrane d_p and Δx can be physically characterized.

One implication of equation (5) is the impact of open area or pore packing density (Θ). This parameter is easy to quantify for straight-through pores as it is a function of the pore cross-sectional area times the number of pores per unit membrane area (equation (6)). For fibrous or other tortuous path pores, it is more difficult to quantify. In this thesis, open area or pore packing density is quantified by the fractional density of the membrane. The fractional density of the membrane is equal to the measured density of the membrane divided by the density of the membrane material (equation (7)) (Nakao Shin-ichi, 1994).

The effect of the fractional density for straight-through pores is to impact the packing density as follows:

$$\Theta = \frac{n \cdot \frac{\pi}{4} \cdot d_p^2}{\text{total surface area}} \quad (6)$$

where n is the number of pores in the exposed membrane area and d_p is the diameter of the pore.

The effect of the fractional density for fibrous or other tortuous path pores is to impact packing density as follows:

$$\Theta = 1 - \left[\frac{\left(\frac{w_m}{\pi \cdot r_m^2 \cdot \Delta x} \right)}{\rho} \right] \quad (7)$$

where r_m is the membrane radius (for a circular membrane), Δx is the membrane thickness, w_m is the weight of the membrane and ρ is the material density.

2.2 Microfabrication of Low Tortuosity Membranes

In the majority of the membrane literature, the morphologies of the membrane is fibrous or tortuous. Track-etched membranes (Kyu-Jin, et al., 1994) can be considered as straight-through pore membranes, but the thicknesses are too thin (less than 10 μm) to be tested and used in heat pump applications.

In the laser micromachining literature, most of the research is concentrated on drilling smaller pores (< 50 μm) of silicon wafer or other metals (Zhao, et al., 1999; Kikuchi, et al., 1997). For heat pump applications, polymer membranes have better characteristics over metal membranes. The main challenge is to fabricate 5 μm pore Kapton (polyimide) membranes with thickness of 50 μm .

Previous results obtained by Dr. Whiteside's research group showed possibilities to fabricate the membrane with arrays of submicron pores using PDMS (Polydimethylsiloxane) (Duffy, et al., 1999; McDonald, et al., 2002). The challenge is to fabricate high aspect ratio membranes and verify the permeability (Jackman, et al, 1999).

2.3 Thesis Statement

The goal of this thesis is to determine what benefit if any straight-through membranes provide

over commercial membranes for mass transfer across contactor membranes. Further, this thesis will demonstrate whether laser micromachining and soft micromolding techniques can be used to fabricate membranes with high aspect ratio pore structures.

CHAPTER 3

Engineered Membrane Design and Fabrication

3.1 Membrane design

To parse the enormous list of commercially available membranes, selection criteria were set relating to the mechanical, flow, and physical characteristics of the membrane. Mechanically, the membrane needed to be stiff to maintain the dimension of adjacent microchannels. With respect to fluid dynamics, the membrane needed to maximize permeability and thereby minimize tortuosity while eliminating breakthrough of the liquid to the gas side of the contactor. To do this, the physical characteristics of the membrane were limited to polymers with thicknesses between 50 and 150 μm and pore size from 1 to 10 μm . After considering all these characteristics, twenty-three membranes were found that met these requirements. Appendix A shows details regarding membrane vendors, materials and morphology.

Two laser micromachined membranes were designed and fabricated. The first one was made at OSU with a nominally 75 μm thick Kapton (polyimide) membrane. The membrane was laser micromachined with an array of 64,516 straight-through holes (254 by 254 holes) with 100 μm pore spacing both vertically and horizontally. Thus, the whole design span one inch by one inch. The second one was made by ESI (Electro Scientific Industries, Inc.) with a nominally 20 μm thick polycarbonate membrane. The membrane was laser micromachined with an array of 258,064 straight-through holes (508 by 508 holes) with 100 μm pore spacing both vertically and horizontally. Thus, the whole design spanned two inch by two inch.

The micromolded membrane was intentionally designed to match the feature from the laser micromachined membranes. The identical feature provides same packing density (open area) which helps when verifying the result during the normalization process.

3.2 Laser Micromachining Approach

3.2.1 Material

To produce a straight-through membrane using laser micromachining, a deep UV laser was used to micromachine an array of pores. The laser used was a fourth-harmonic Nd:YAG laser outputting a TEM (1,0) beam at a wavelength of 266 nm. The beam shape was characterized by a Spiricon laser beam analyzer (LBA-400PC). In order to obtain better quality straight-through pores, both polycarbonate and polyimide (Kapton) film were tested. Preliminary results showed that Kapton films have less thermal effect than polycarbonate films.

3.2.2 Method

Gaussian laser beams have two major characteristics. One characteristic is the effective beam radius, $\omega(z)$, defined by the waist of the beam at $1/e^2$ (13%) of the peak beam intensity. The other key characteristic is the radiated angle, $2\theta_a$. These beam properties are portrayed in Figure 1. The effective beam waist controls the pore size in the laser machining process. The radiated angle affects the beam waist with respect to the distance between the focusing lens and the workpiece material (the working distance).

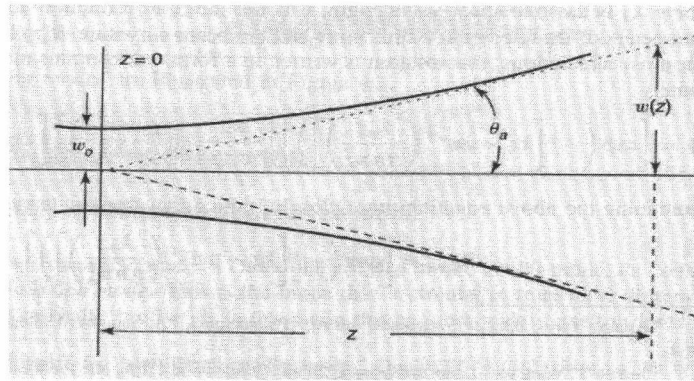


Figure 1: Gaussian beam properties (Source: Laser Engineering, Keln J. Kuhn, 1998)

A critical parameter for consistently producing 5-15 micron holes across the surface of the membrane is the depth of field (Z_R) (Kuhn, 1998). The Gaussian beam expands rapidly beyond two times of the depth of field region. One half of the depth of field can be calculated as follows:

$$Z_R = \frac{\lambda_0 f^2}{\pi n (\omega(f))^2} \quad (9)$$

where λ_0 is the wavelength of the laser, f is the focal length of the focusing lens and $\omega(f)$ is the laser beam waist before going through the focusing lens. The beam was focused down through a 0.5-inch focus lens to the material surface.

From equation (9), assuming a 266 nm laser, a 0.5-inch focal length lens and an incident beam diameter of 1 mm, one half of the depth of field is found to be 53 microns. Therefore, theoretically, the total depth of field under laboratory conditions is only 106 μm . Therefore, the depth of the material used in this study was significantly less than 100 μm . Also, in order to consistently machine the material, a repeatable procedure was developed to focus the laser beam onto the workpiece surface. In addition, efforts were made to reduce the flatness of the workpiece material to within 100 μm .

3.2.2.1 Focusing procedure

As the distance between the workpiece and objective lens extends beyond the focal plane, the laser beam waist expands (Figure 1). Therefore, a procedure was established to consistently focus the laser beam on the midplane of the material. The focusing procedure involved two major steps. The first

step was to find the focus of the laser at the material surface. The second step involved bringing the focal point of the laser to the material midplane (half the height of the material).

The first step of this procedure was executed by machining a series of holes; each individual hole was machined at a different working distance from the objective lens. By examining the hole patterns through a microscope, the proper working distance of the laser could be determined. Figure 2 depicts the hole patterns with 200 μm of height variance between holes. Based on the result from 200 μm height variance, the next step was to find the best hole patterns by 20 μm height variance (Figure 3).

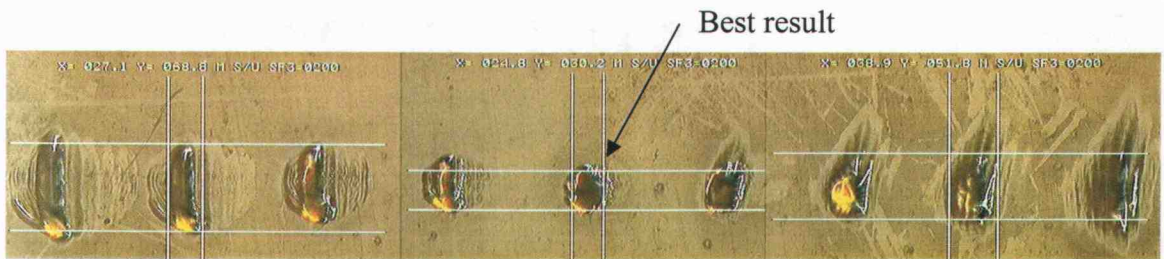


Figure 2: Hole patterns with 200 μm height variance



Figure 3: Hole patterns with 20 μm height variance

After finding the focal point on the material surface, an adjustment was made to raise the stage half the height of the material to minimize the beam spread as it passed through the material. Appendix B gives a protocol for focusing the laser beam.

3.2.2.2 Parallelism of workpiece

By using a similar technique as the focusing procedure, a hole pattern was made at each of the four corners and the center point of the workpiece to check the parallelism of the workpiece with respect to the focal plane. The parallelism of the workpiece was determined by inspecting the variation of the dimension of the holes of the hole patterns by a microscope. From formula (9), assuming the incoming laser beam was perpendicular to the workpiece and had uniform shape, the only element that can cause the shape variance is the difference of the working distance (Z_R) which relate to parallelism of the workpiece. Test results show the ability to hold a hole size variation of 4.98% across the workpiece which translates into a parallelism of the workpiece. Appendix C gives a protocol for verifying the workpiece flatness.

3.2.2.3 Beam profile

One other critical parameter to this work was the profile of the beam. The more Gaussian the beam shape, the more circular the hole. The spatial distribution of the beam was found to be TEM 1,0 with the use of a beam profiler (shown in Figure 4 and Figure 5). Much of the cause of the beam imperfections is due to the non-linear crystals used to double and quadruple the photon energy. The beam profile was found to change as a function of the amperage provided to the laser power supply. Figure 4 and Figure 5 show the 3-D and 2-D view of the laser profile as measured by the beam profiler at 18 and 17 amps, respectively. It was found that the beam profile emulated a TEM 0,0 beam at around 17 amps. Because of this fluctuation in beam shape, the beam profile was verified both before and after machining to ensure repeatability. This beam profile was found suitable for drilling 5~15 micron holes in Kapton.

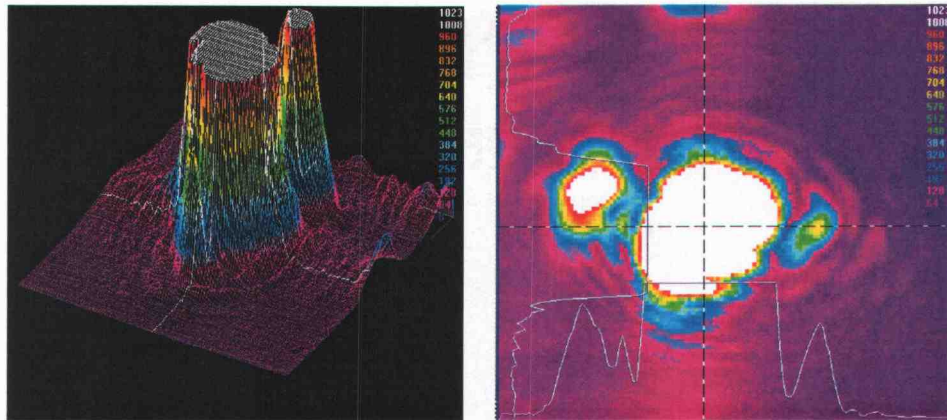


Figure 4: 3-D and 2-D view of laser profile at 18 amps

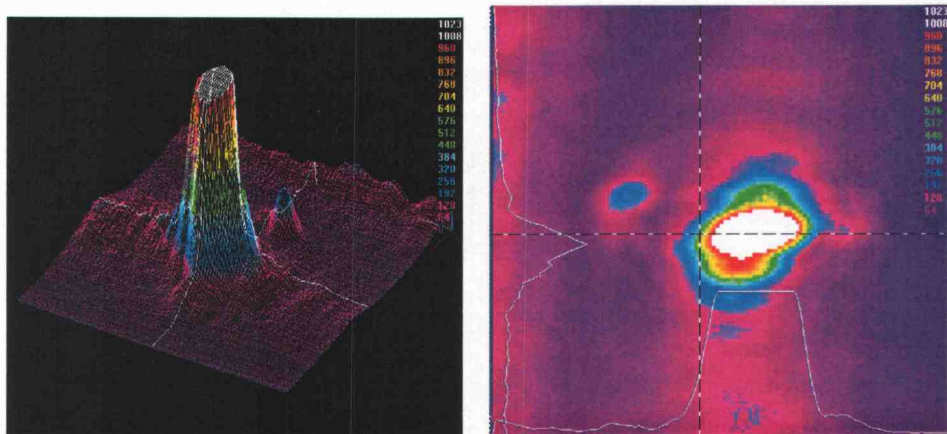


Figure 5: 3-D and 2-D view of laser profile at 17 amps.

3.2.3 ESI

Electro Scientific Industries, Inc. (ESI) is a company who supplies high-value, high-technology equipment to the global electronics market. Founded in 1944, the ESI's success as a company is based on a foundation of core principles: financial strength, global reach, people values and technology. ESI have manufacturing facilities in Oregon which provides much needed help to produce the laser micromachined polycarbonate membranes. This membrane was later verified and compared to the membrane micromachined in OSU.

3.3 Micromolded Approach

3.3.1 Material

To produce a high aspect ratio micromolded membrane, a soft lithography technique was used to produce an elastomeric membrane. PDMS (Polydimethylsiloxane) was micromolded using patterned thick resist (SU8) to create an engineered membrane.

3.3.1.1 PDMS

PDMS is a synthetic polymer with elastic properties similar to that of rubber and is considered an elastomer. Its structural formula is as shown in Figure 6 where n can be on the order of thousands. Molecular weights of PDMS can reach 700,000 or higher.

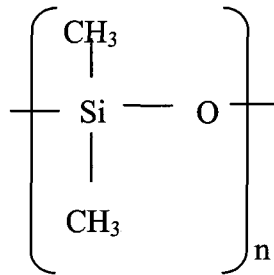


Figure 6: Structural formula of PDMS.

The PDMS being used in this micromolding process is Dow Corning Sylgard 184. It is supplied as two constituents: the base oligomer (that contains vinyl-terminated dimethyl siloxane and a platinum catalyst) and the cross-linker (hydride – terminated dimethyl siloxane). The platinum-catalyzed addition reaction between the vinyl functional group ($\text{SiCH}=\text{CH}_2$) of the base oligomer and the hydride functional group (SiH) of the cross-linker results in the curing of a mixture of the two constituents. This reaction is known as hydrosilylation (hydrosilation). The normal mixing ratio of the base oligomer to cross-linker is 10:1, however, one can vary the mixing ratio to achieve a desired

strength of the cured PDMS. Cured PDMS is stable and flexible from $-50\text{ }^{\circ}\text{C}$ to $+200\text{ }^{\circ}\text{C}$.

3.3.1.2 SU8

SU-8 2000 (formulated in cyclopentanone solvent) is a chemically-amplified, epoxy-based negative photoresist. Standard formulations are offered to cover a wide range of film thicknesses from 1 to 200 μm . SU-8 2000 resist has high functionality, high optical transparency and is photosensitive to near UV radiation. Images having exceptionally high aspect ratios and straight sidewalls are readily formed in thick films by contact-proximity or projection printing. Cured SU-8 2000 is highly resistant to solvents, acids and bases and has excellent thermal stability, making it well suited for applications in which cured structures are a permanent part of the device. Regarding the thickness of the membrane, the formulation that this thesis used was SU8 2050 which provides a thickness around $50\mu\text{m}$.

3.3.1.3 Substrate Selection

Glass slides and silicon wafers were evaluated for their suitability as SU8 substrates during spincoating. An adhesive promoter was also used to improve adhesion. Though glass substrates are cheaper, the experimental results in Figure 7 indicate that silicon wafers work better as SU8 substrates. The photomask used for the pattern in Figure 7 included an array of holes consisting of 5-micron diameter holes on a $100\text{ }\mu\text{m}$ grid horizontally and vertically.

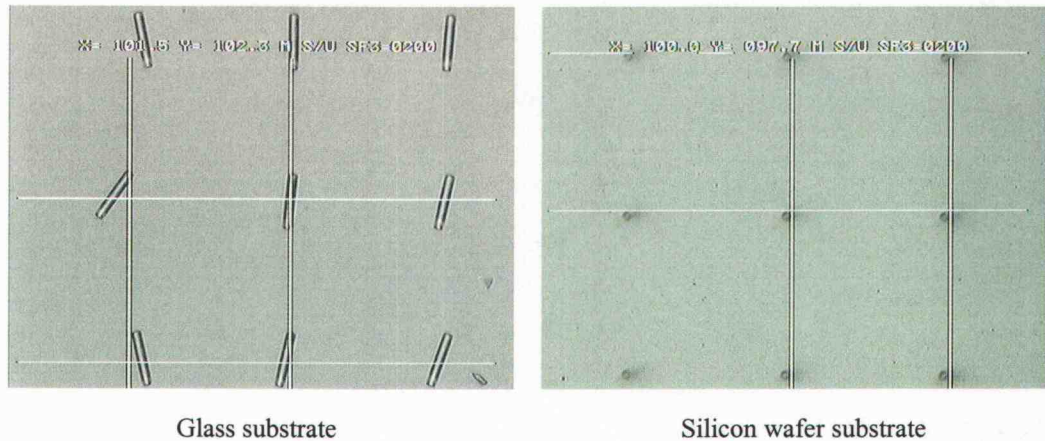


Figure 7: Comparison between glass and silicon substrate. (Adhesion promoter was used in both instances)

3.3.1.4 PEG sacrificial layer

To release the PDMS membranes from SU8 micromolds, PEG (Polyethylene Glycol) was used as a sacrificial layer. Methonal was used to dissolve the PEG powder with a ratio of 10:1 (10g of Methonal to 1g of PEG). The PEG solution was then spincoated on the silicon wafer with SU8 posts at 6000 rpm for 1 minute. The thickness of the PEG was approximately 2 to 5 μm . The reason for implementing this process was because the SU8 posts tend to break off from substrate during separation of the membrane from the micromold. A sacrificial layer added in between SU8 and PDMS can assist the membrane to release from the SU8 posts. To release the PDMS membrane, the whole substrate was submersed into DI water and ultrasonicated for 30 minutes. The PEG coating was dissolved and the PDMS membrane separated from the silicon wafer and SU8 posts.

3.3.2 Method

The PDMS membrane fabrication process can be divided into four major steps (Figure 8). The first step is to create SU8 posts on the substrate. The second step is to spincoat PDMS onto the substrate

with SU8 posts in order to mold PDMS membranes with straight through pores. The third step is to spincoat a thin sacrificial layer of PEG. The fourth step is to separate the PDMS membrane from the SU8 mold and substrate. The permeability was evaluated from the test loop.

The silicon wafer was first immersed in etching solution (10% of HF and 90% of deionized water) to etch the silicon oxides before the spin coating process. To obtain maximum process reliability, the substrate needs to be clean and dry prior to applying the SU8 resist. The Si substrate is first rinsed with Acetone, Methanol and DI water to remove organic residuals. Then the Si substrate is etched for 10 minutes by using an etching solution (10% of HF and 90% of deionized water). After the etching process, the Si substrate was put into a hot plate oven for 15 minutes at 150°C to dehydrate the surface. Adhesion promoters (MicroChem's OmniCoat) was then spin coated on to the surface with 3000 rpm for 30 seconds. The substrate was then put into the oven for one minute at 100°C. Both the etching process and adding the adhesive promoter will help the structure to stay on the Si wafer surface.

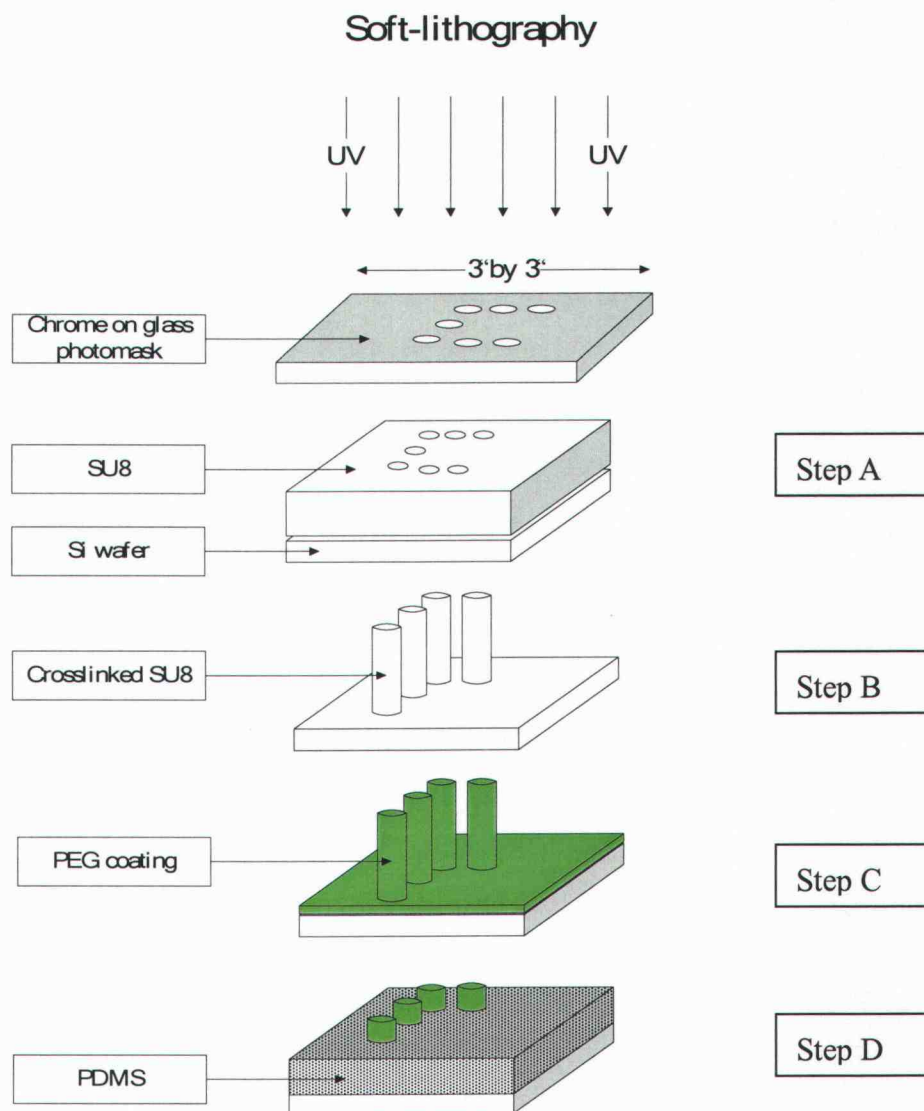


Figure 8: Schematic of process steps for PDMS membrane fabrication

The SU8 was then spincoated onto a Silicon wafer. From MicroChem's recommended coating conditions, 1 ml of SU8 per inch of substrate diameter should be used. For a 3-inch diameter Si wafer, 8 ml of SU8 was applied to the wafer. MicroChem also suggests using two steps to spin coat SU8. In the spread cycle, the coating machine was first ramped up to 500 rpm at 100 rpm/second acceleration and then the speed was held for 5-10 seconds to cover the entire surface. After the spread cycle was complete, the coating machine was ramped to final spin speed at an acceleration of 300 rpm/second and held for a total of 30 seconds.

After the resist is applied to the substrate, it must be soft baked to evaporate the solvent and densify the film. MicroChem recommends the bake time for 60- μm thickness to be 3 minutes of pre-bake at 65°C then 9 minutes of softbake at 95 °C.

The photomask was then placed directly on the SU8, preceded by going through the i-line exposure tool for 15 minutes (Step A on Figure 8). The recommended dosage for 60- μm thickness is around 250 mJ/cm². The SU8 exposed from the UV was crosslinked.

Following exposure, a post exposure bake (PEB) must be performed to selectively cross-link the exposed portions of the film. The substrate is pre-PEB for 1 minute at 65°C then PEB for 7 minutes at 95 °C in a hot plate oven.

The substrate is then immersed in MicroChem's SU8 Developer for developing. The uncrosslinked SU8 was removed under developer (Step B on Figure 8). The substrate is fixed in the glass container and the container is placed on the magnetic stirrer. Stirring the developer helped to achieve high aspect ratio structure.

The SU8 posts was then spin coated with a sacrificial layer using polyethylene glycol (Step C on Figure 8). This prevent the PDMS (Polydimethyl siloxane) to have direct contact with the SU8 posts and ready the PDMS to perform the lift-off process (Step D on Figure 8). The lift-off process was performed by putting the substrate into the ultrasonicator with Deionized water and Iso-Propyl Alcohol. The PEG was dissolved in the solution to release the PDMS from Si substrate and SU8 post structure.

CHAPTER 4

EXPERIMENTAL APPROACH

4.1 Baseline Measurements

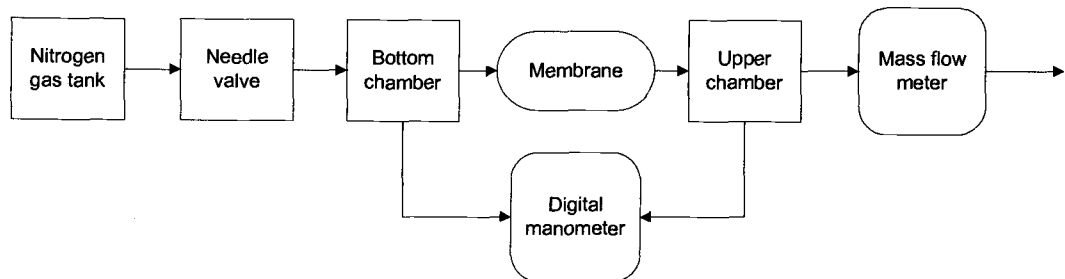


Figure 9: A simple schematic of the membrane mass flux test loop.

To measure mass transfer performance, a pressure drop test loop capable of measuring the pressure drop across a membrane as a function of mass flux was developed. As shown in Figure 9 and Figure 10, the experimental setup for conducting the pressure drop testing across the conventional membranes involved flowing nitrogen from a tank through a needle valve (flow rate control) and into the lower plenum of a test fixture. Once in the test fixture, the nitrogen flowed across the membrane and into the upper plenum of the test fixture. The test fixture was necessary to ensure flow across a constant cross-section of each membrane. The diameter of the upper plenum was 2.0 inches while the lower plenum had a diameter of 0.4 inches. A stiffener was added to prevent the membranes from deflecting. The stiffener was 500 microns thick made from partially sintered stainless steel powder with a final pore size of 100 micron. A picture of the test fixture including gaskets and stiffener is shown in Figure 11. An OMEGA HHP-2000 digital manometer was used to measure pressure drop between the upper and lower plenums. A MKS Type M10MB (M10MB13CS3BV) mass flow meter was connected to the

test loop at the output of the upper plenum. The test loop was designed to permit no more than 5% uncertainty in pressure drop (between 2 and 18 torr) and mass flux (between 200 and 1000 sccm).

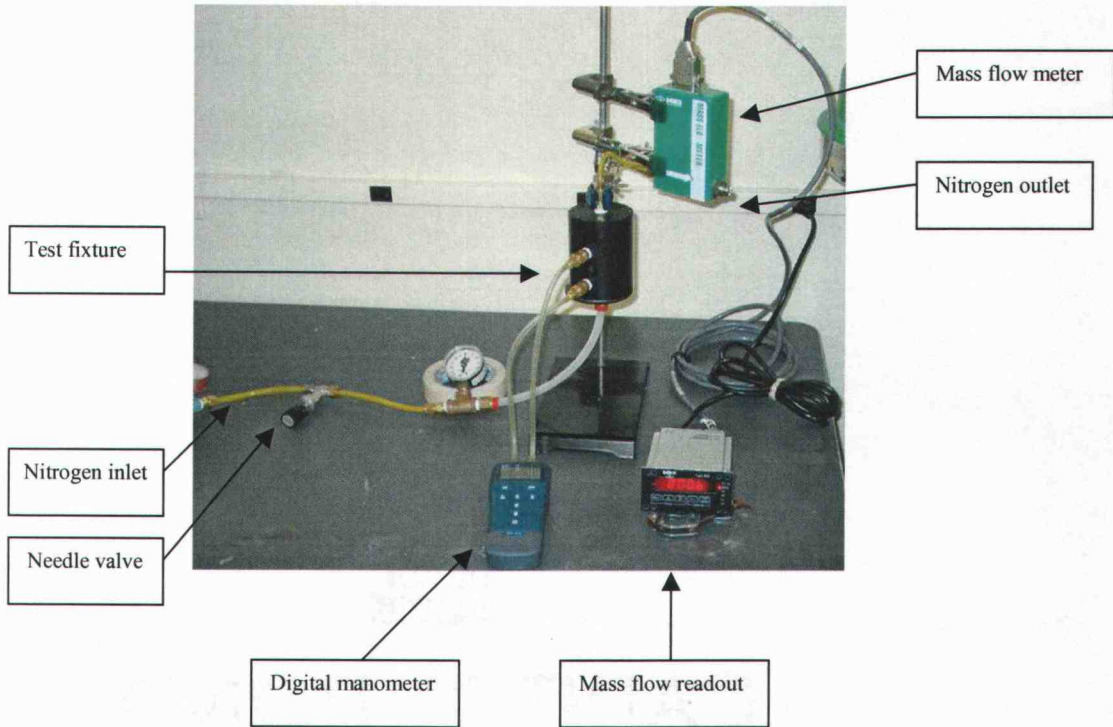


Figure 10: Physical layout of the membrane mass flux test loop.

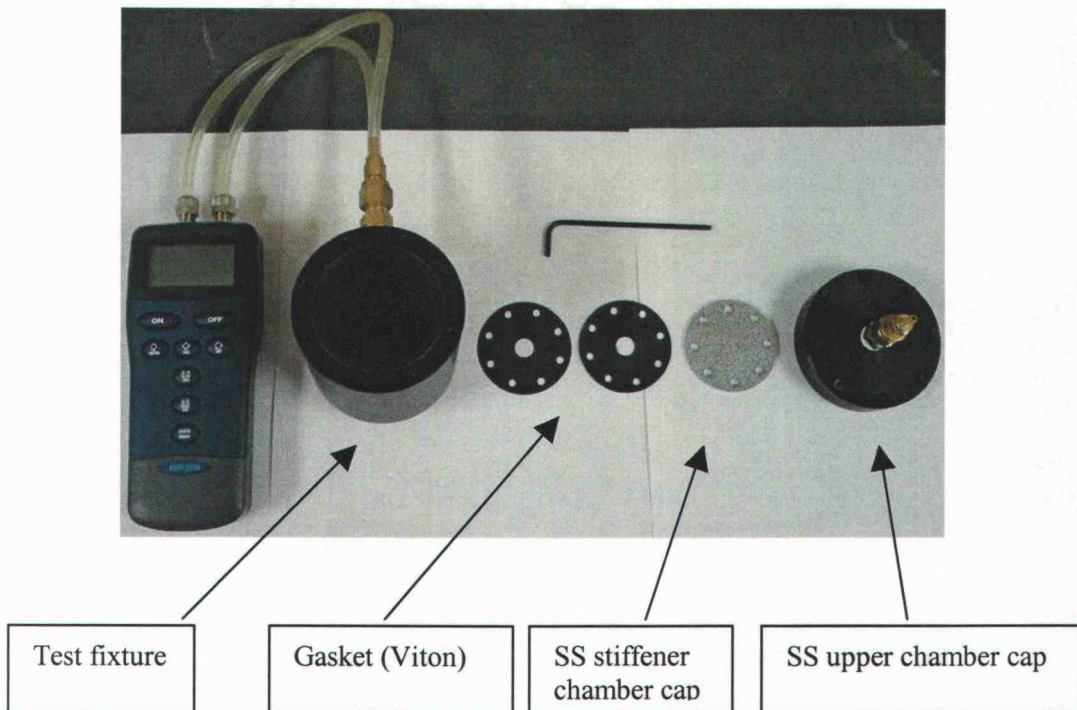


Figure 11: Physical layout of the membrane mass flux test fixture.

The protocol used to test each membrane involved securing the membrane within the test fixture using a SS stiffener (see Figure 11). The testing protocol involved opening the upper plenum cover and removing the SS stiffener along with the Viton gaskets. The test membrane was placed between the test gaskets and the stiffener/gasket/membrane assembly was reinstalled within the test fixture. The test was performed by first running the experiment up to the maximum recordable pressure drop or flow rate and then back down to zero. Between five and ten data points were collected in both directions. The specific procedure for testing membranes can be found in Appendix D.

In all, 27 commercial membranes had been obtained and 27 membranes were tested on the test loop. The repeatability of the test loop results are less than 7% of error (Appendix F).

4.2 Experimental approach for laser micromachining and micromolded membrane

Two laser micromachined membranes (OSU and ESI) have been fabricated. A test sample of 0.5 inch by 0.5 inch were cut from the membrane and tested with the test loop. The micromolded membranes were fabricated and characterized. To manipulate the thin PDMS membrane, IPA was applied to swell the membrane and reduce friction from the substrate. Toluene can also be applied to the membrane to swell the membrane even more by 50% than its original size.

CHAPTER 5

RESULTS AND DISCUSSION

5.1 Mass Flux Results for Commercial Membranes

5.1.1 Baseline Results

Figure 12 shows results as a function of the average pressure drop and mass flux across for each membrane. These are raw data results and do not represent normalized data. Notice that the leftmost data plot shows the mass flux characteristics of the test fixture without a membrane.

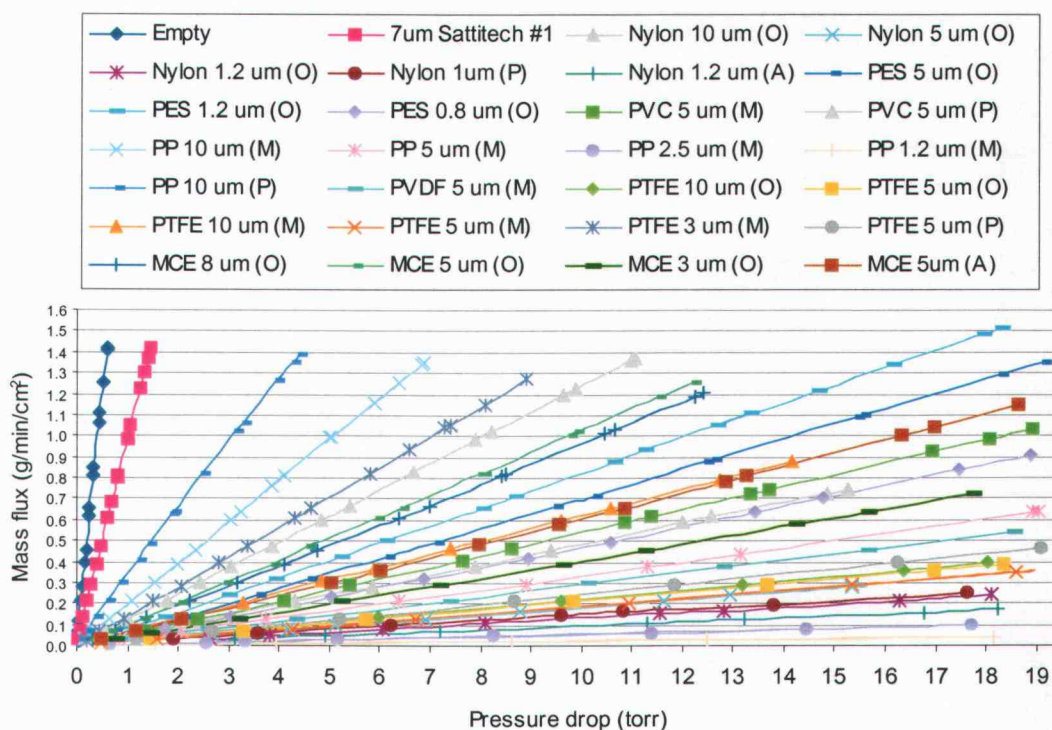


Figure 12: Average pressure drop results as a function of mass flux across the baseline membranes.

5.1.2 Normalized Results for Non-Engineered Membranes

By normalizing the experiment data using Equation (5), the result is shown on Figure 13.

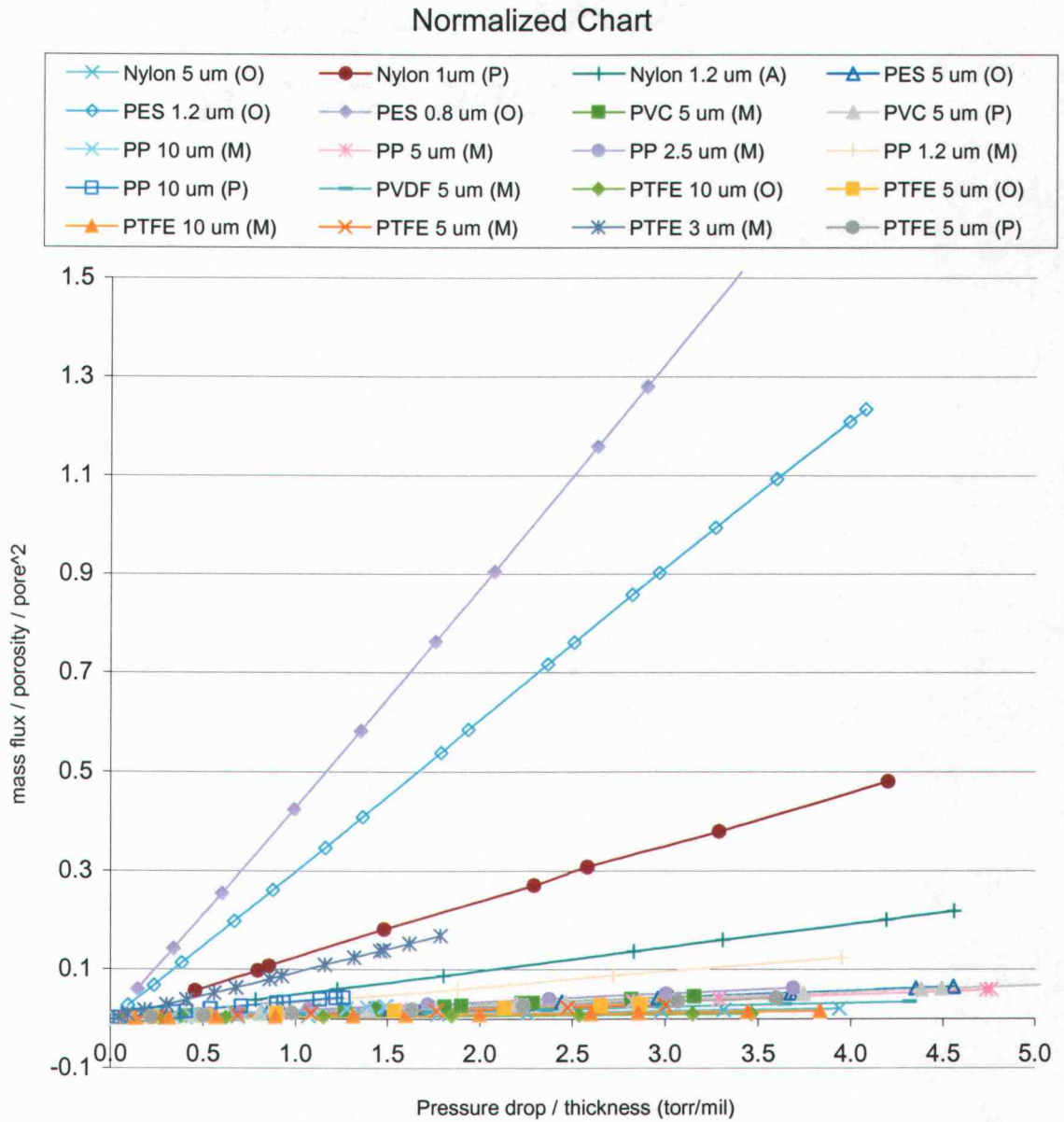


Figure 13: Normalized pressure drop results as a function of normalized mass flux across the baseline membranes.

From the results, it is apparent that certain membrane morphologies exhibit better mass flux properties than others. Two of the membranes which stand out are the PES membranes with 0.8 and 1.2 μm pore sizes. The performance of these two membranes indicates that there is something different about the morphology of these membranes that provide better mass flux characteristics (Quartarone, et al., 2002). While the performance of these membranes stands out from the rest, its performance is not as exceptional as the other membranes. The pressure drop across these membranes is about two times less than that of the nearest remaining membrane.

Normalization was not performed for the MCE membranes because the material density data was not available. However, based on the morphology of the membranes, it is expected that it would also reside in the lower performing membranes particularly in light of their poor average performance in **Figure 13**.

To expand upon the observations above, an analysis of the effects of morphology and pore size on the performance of the membranes was performed. Reviewing Appendix A, the membrane morphologies can be classified into three broad categories: networked, fibrous, and tortuous. Networked membranes differ from fibrous and tortuous membranes in that the membrane is an interconnected web of material while fibrous membranes are not connected with one another. One difference in fibrous and tortuous morphologies is that fibrous and tortuous morphology may result in “dead ends” or flow terminations as the fluid winds through the structure. Networked morphologies are incapable of terminating flow paths. Therefore, it is plausible that the tortuous structures could provide higher pressure drops than other structures.

Figure 14 shows the same normalized graph plotted for the three different morphologies investigated in the mass flux baseline. This supports the notion that in general, networked morphologies provide less pressure drop than fibrous and tortuous morphologies though need more understandings on PES morphologies.

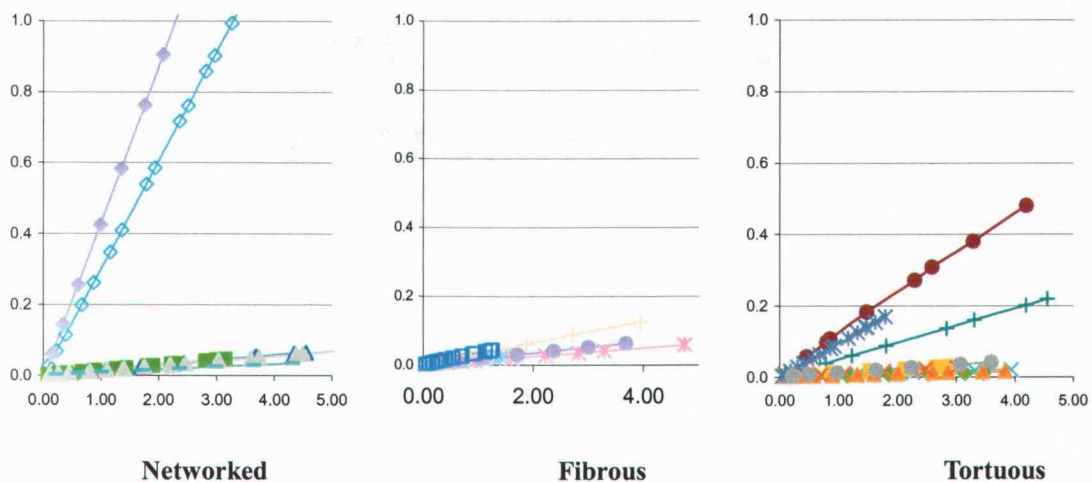


Figure 14: Normalized pressure drop results for networked, fibrous, and tortuous structures

Figure 15 shows the same normalized plot from the perspective of pore size. As shown, only the smaller pore sizes such as PES tends to give better results.. It is possible that the fluid dynamics are significantly different with membranes having smaller pore sizes so that even though the data has been normalized.

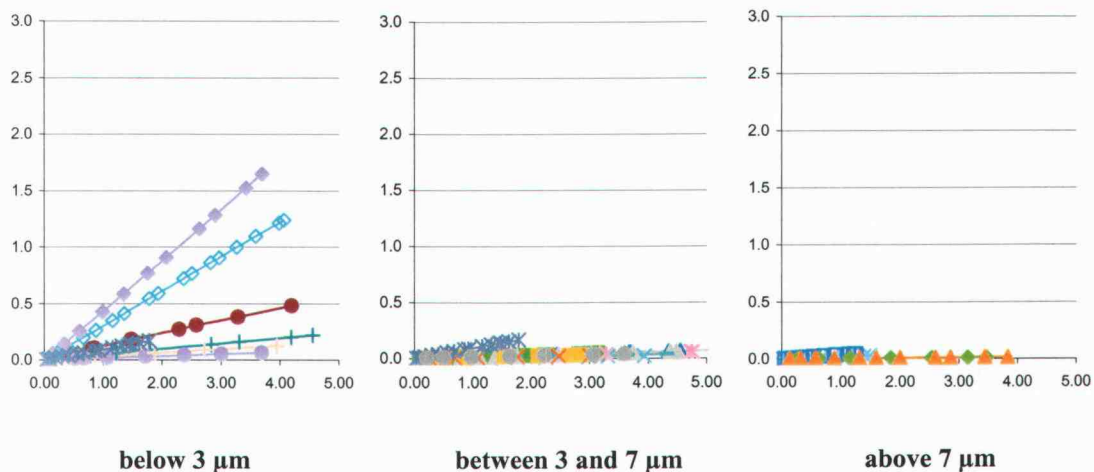


Figure 15: Normalized pressure drop results for different pore size structures

5.1.3 Normalized Results for Woven Membranes

One of the commercial membranes that was different from the rest was the Sattitech woven membrane. Figure 40 compares the 7 μm woven membrane with the other 5 to 10 μm commercial membranes. The Sattitech 7 μm pore membrane is a woven membrane with straight-through pores and clearly exhibits the best mass flux properties. The superior performance may be due to the fact that flow paths are not simply limited to the open area but that additional flow paths between woven fibers permit additional mass flow. In addition, it was quite difficult to estimate membrane thickness and porosity for this membrane. To test the actual performance of the membrane as a contactor, additional breakthrough tests should be performed. The 7 μm pore size is anticipated to be too large for breakthrough tests. At this time, the pore size for woven membranes cannot extend below 7 μm . It will be interesting to find out if there exists a limit on the smallest, repeatable pore size possible by woven membranes.

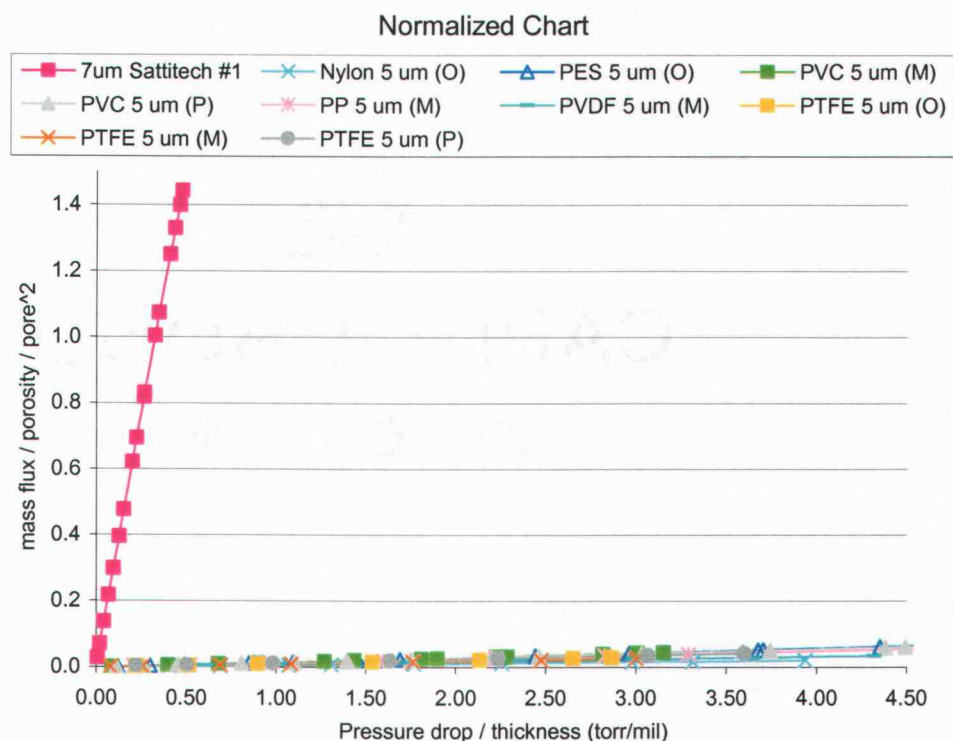


Figure 16: Comparison of woven membrane with commercial membranes with similar pore size.

5.2 Laser Micromachining Membrane Results

5.2.1 Laser Micromachined Membranes

For the laser-micromachined membranes produced at OSU, the average pore size was found to be different on the front side than on the back side of the material due to the characteristic parabolic shape of the laser energy deposition. The test results were verified via the procedure described in Appendix G. Figures 17 and 18 show the front and back sides, respectively, of the Kapton membrane (laser micromachined by OSU). By randomly sampling 30 different holes using optical microscopy, the average pore size was found to be $16.5 \pm 0.5 \mu\text{m}$ for the front side and 5.3 ± 0.8 for the back side.



Figure 17: Front side pore array with $100 \mu\text{m}$ spacing and average pore size of $16.5 \pm 0.5 \mu\text{m}$



Figure 18: Back side pore array with 100 μm spacing and average pore size of $5.3 \pm 0.8 \mu\text{m}$.

Figures 19 and 20 show the front and back side of the polycarbonate membranes made by ESI. By randomly sampling 30 different holes using optical microscopy, the average pore size was found to be $16.5 \pm 0.5 \mu\text{m}$ for the front side and 5.3 ± 0.8 for the back side.



Figure 19: Front side of the Polycarbonate pore with 200X

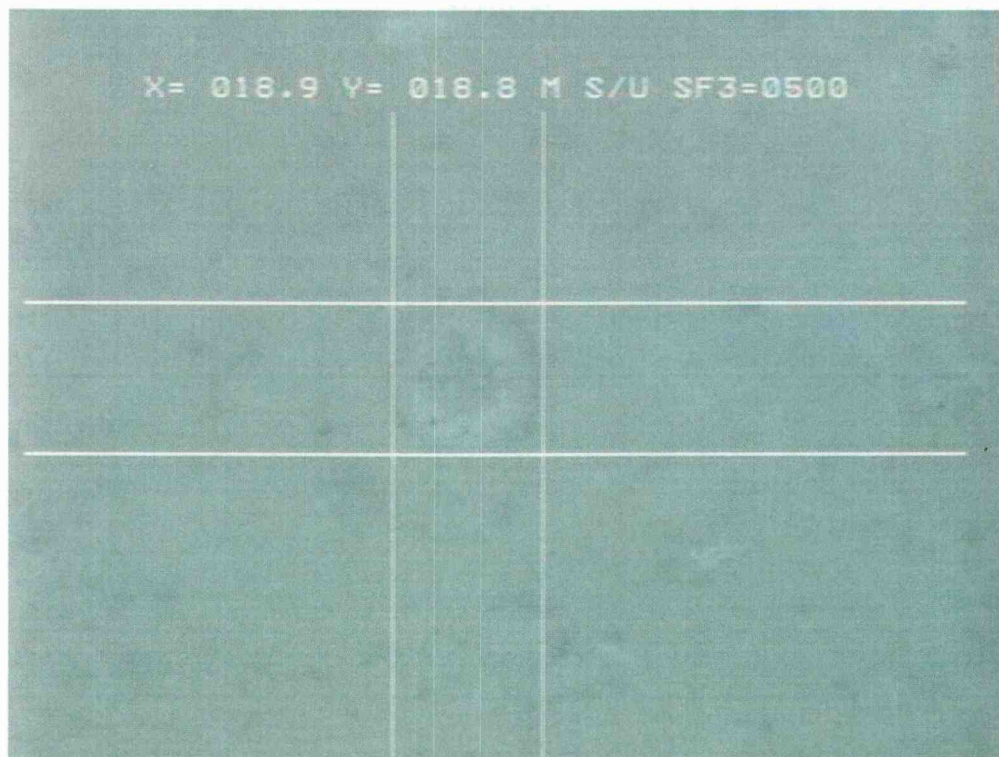


Figure 20: Back side of the Polycarbonate pore with 500X

5.2.2 Normalized Results for Laser Micromachined Membrane

The laser micromachined membranes were flow tested using the same test loop and procedure as before. Figure 21 shows the normalized results of the laser micromachined membranes with respect to the baseline of commercialized membranes shown in Figure 16. The mass flux results of the laser micromachined membrane shows a significant improvement over the commercial fibrous and tortuous membranes. This along with the performance of the woven membrane verifies that straight through pores have superior mass flux performance as compared to the bulk of the networked, fibrous and tortuous membranes. The one exception is the PES membranes which also show similar mass flux performance.

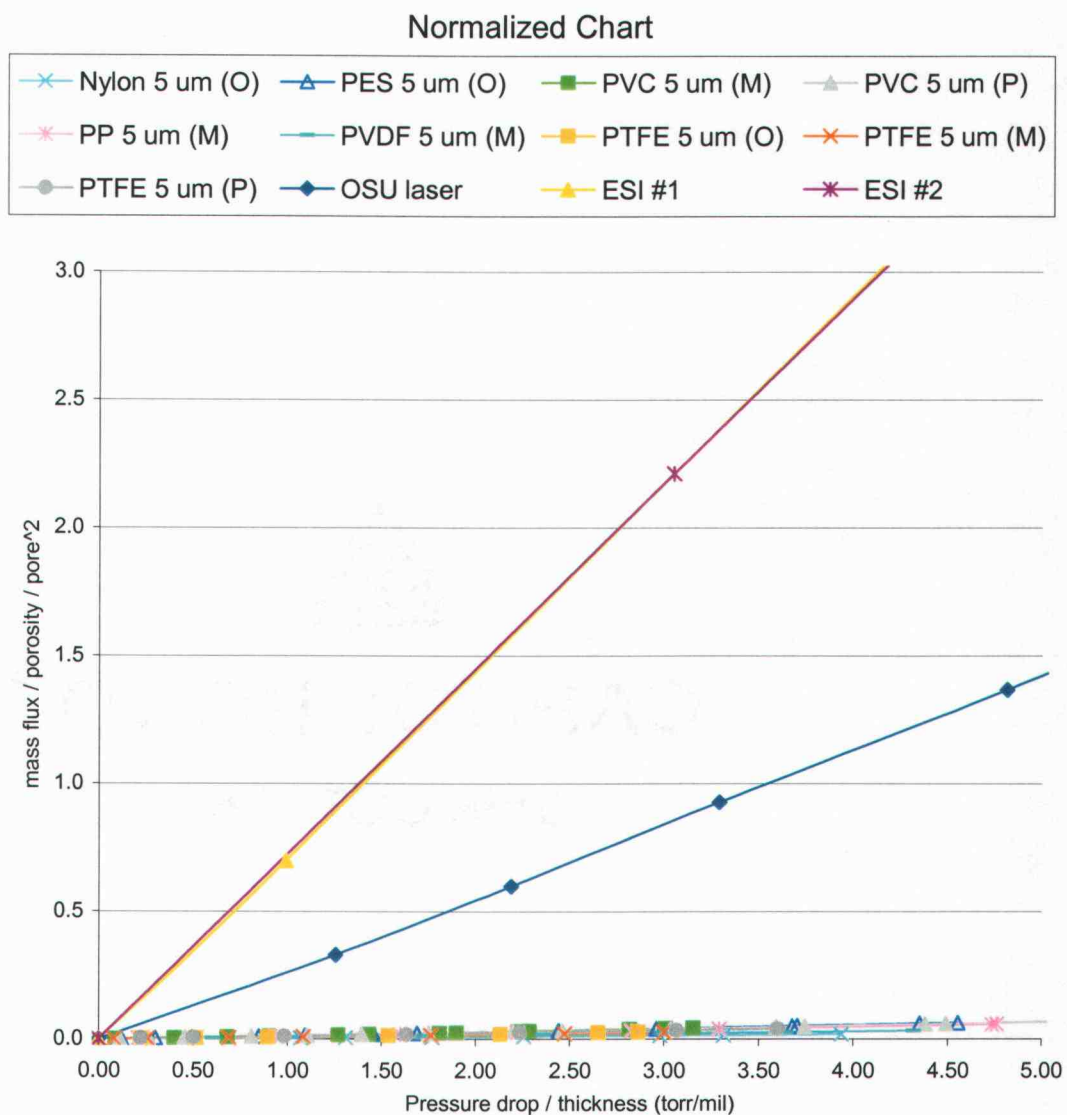
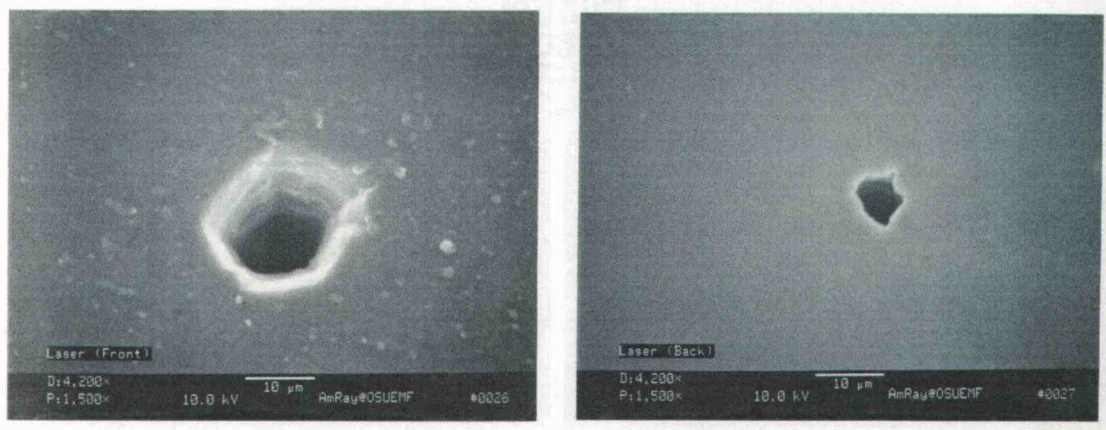


Figure 21: Normalized mass flux results for the laser micromachined membranes compared with

Figure 16.

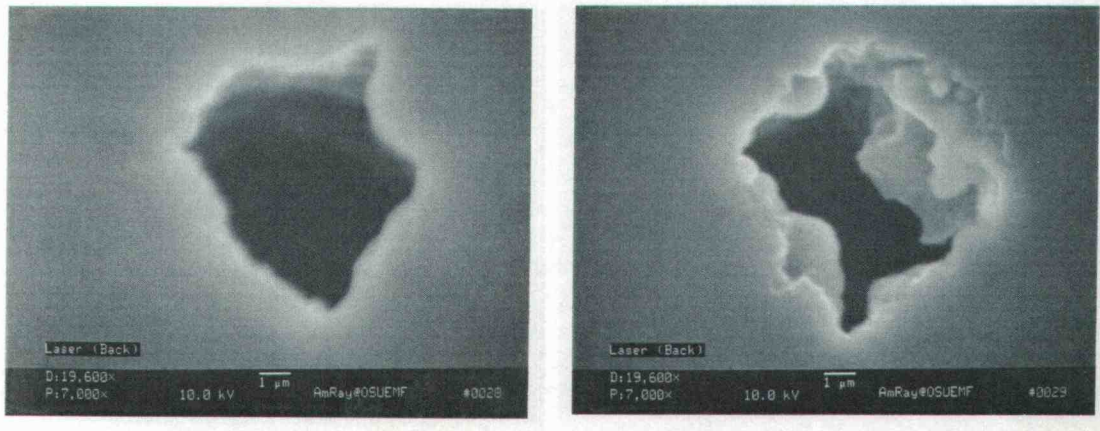
Several characteristics of the laser machined membranes were analyzed to infer relationships between the structure of the membranes and their performance. First, as can be seen in Figure 22, the laser ablation process is a thermal process. Therefore it is expected that in some of the pores, the surface roughness on the inside of the hole is greater than the surface roughness of either the tortuous or the fibrous membranes. In other words, pores that have rough surface roughness have more pressure drop than pores that have smooth surface roughness. Figure 22 provides some support indicating that the pore shape departed from being circular through the length of the pore. Figure 23 suggests that the backside exit of the pore particularly showed an observable level of roughness inside the pore.



Frontside of the pore (1500X)

Backside of the pore (1500X)

Figure 22: SEM Pictures of Frontside and Backside of the pore



Smooth Backside Pore (7000X)

Rough Backside pore (7000X)

Figure 23: SEM pictures showing evidence of surface roughness just inside the backside pore exit.

Another source of increased tortuosity might have been a variation in pore size. While the initial results of pore size across the membrane are encouraging, it is impossible to check all 22,500 pores on the membrane. Prior tests have shown that if the membrane is not within its required parallelism, the out-of-focus can cause large variations in pore size including elimination of the pores altogether.

Future tests will emphasize improvements in the laser micromachining procedure by lifting the workpiece material off of the vacuum chuck to help increase flatness and minimize heat affects. Further, several membranes will be made with varying pore array densities to analyze the effect of packing density on the mass flux of membranes.

5.4 Permeability Versus Porosity, Thickness, and Pore Size

To further differentiate the advantages of the engineered membranes, several additional contactor membrane requirements were considered. From the contactor requirement mentioned before, stiff contactors are preferred inside the heat pump. While membrane stiffness was not specifically

measured in this study, general characteristics of the membrane were used to make inferences concerning membrane stiffness. Membranes with higher porosity tend to have less stiffness. Therefore, Figure 24 shows the permeability with respect of porosity. Desirable membranes would be in the bottom, left quadrant. In this graph, the engineered membranes stand out from the rest. Further, the laser machined membranes are shown to be potentially much stiffer than the woven membranes due to more material.

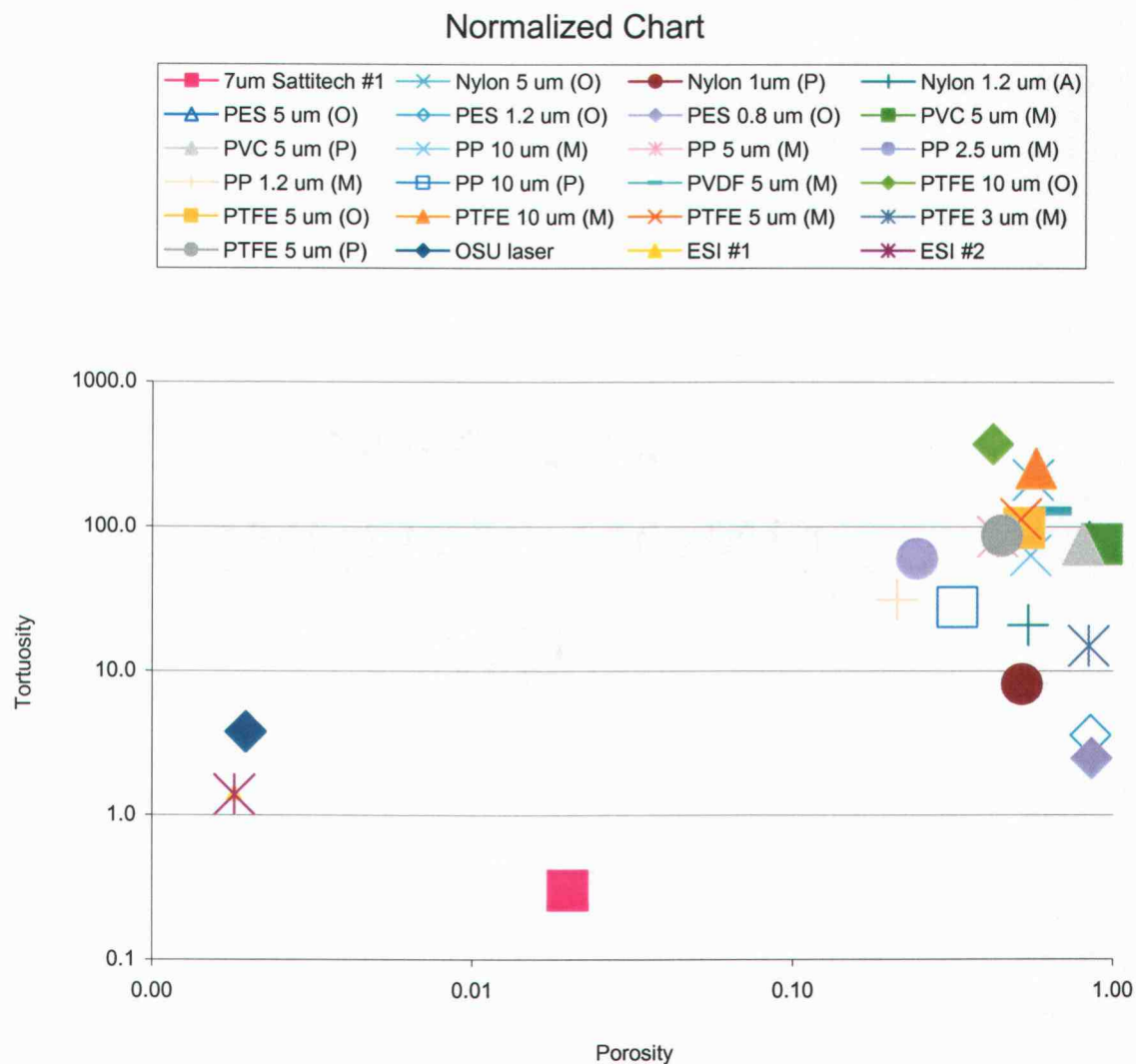


Figure 24: Tortuosity versus porosity plot. Membranes found in the lower, left quadrant would tend to have higher permeability with lower stiffness.

The plot of membrane tortuosity and thickness is shown on Figure 25. The laser micromachined membrane by ESI has the thinnest thickness but by increasing 254% of the thickness (OSU membrane) the tortuosity is still low comparing with other membranes. In all, considering that solid sheets of material would be expected to be much stiffer than woven sheets, the circumstantial evidence suggests that the laser machined approach would provide much better stiffness at improved permeabilities.

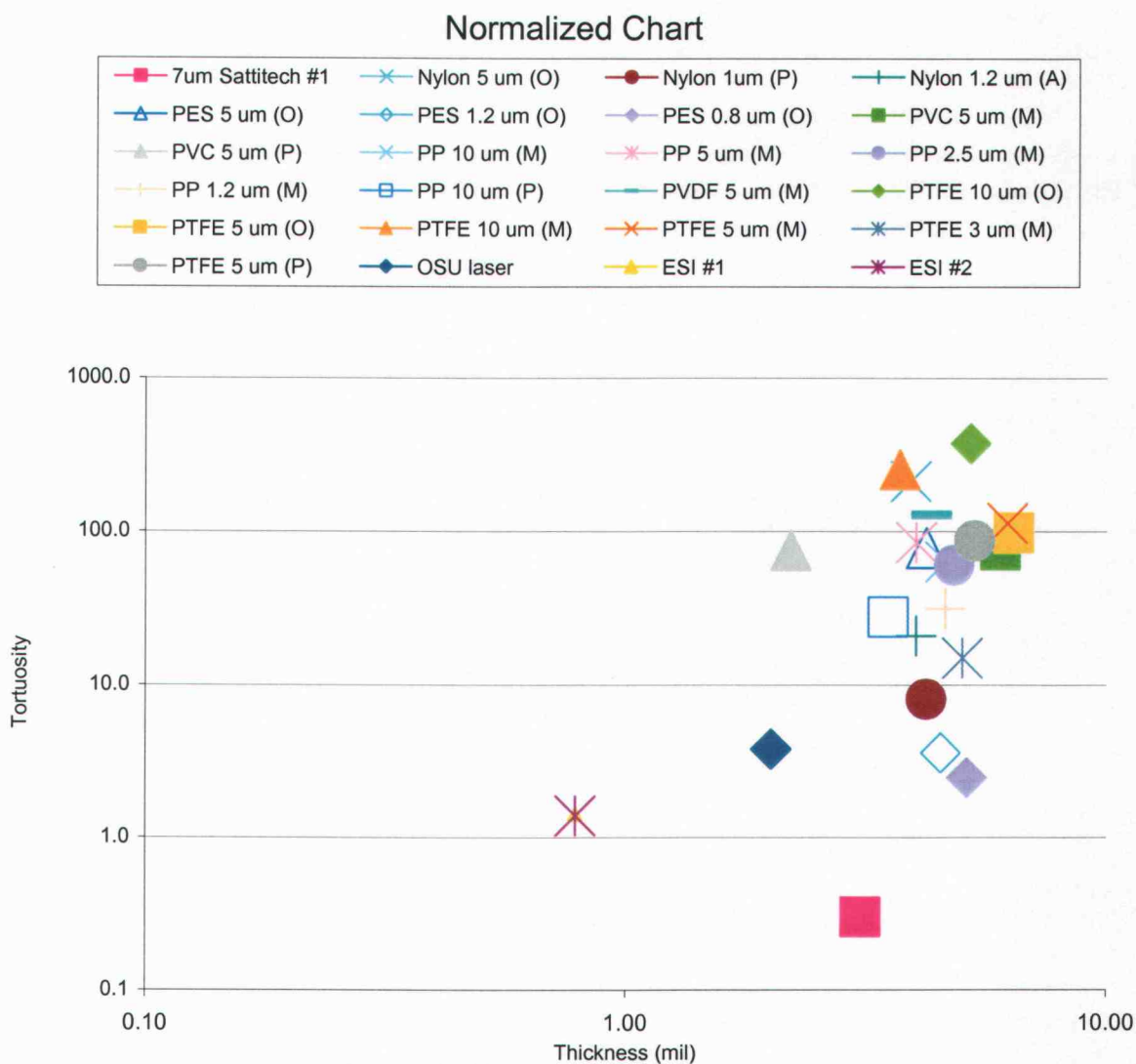


Figure 25: Tortuosity versus Thickness

Breakthrough of liquids into gases through contactor membranes has to do with pore size as

well as the hydrophobicity of the membrane. Accordingly, Figure 26 shows that the woven membranes may have breakthrough problems since the size of the pores cannot currently be made below 7 μm . It is expected that the pore sizes of laser machined membranes can be further reduced.

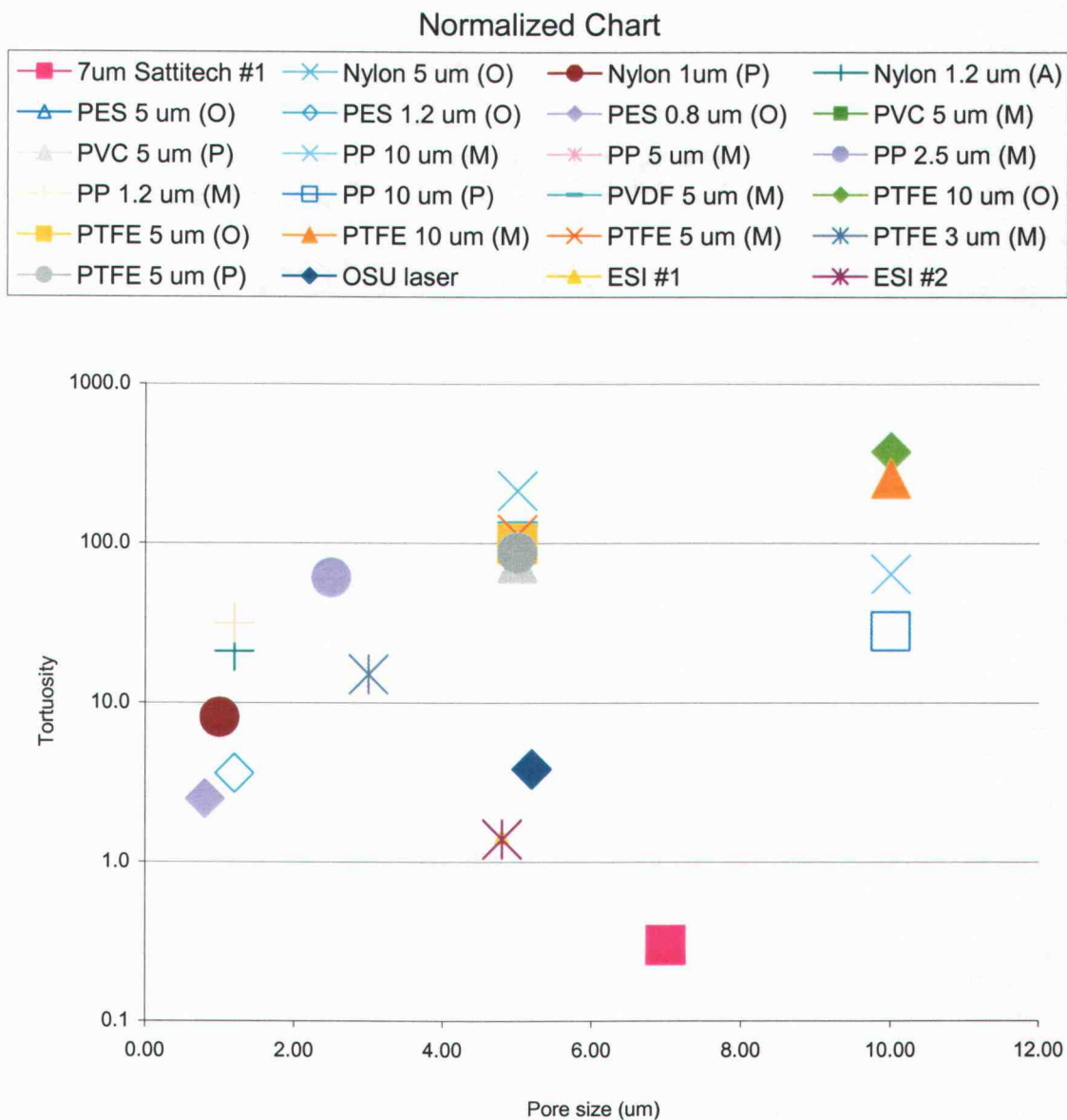


Figure 26: Permeability versus Pore Size

In the end, these charts indicate that laser-machined membranes provide some opportunities for increasing the permeability of commercially available membranes, while also meeting the additional stiffness and breakthrough requirements of membranes. Additional testing is needed to verify this.

One trend in the data is that as membrane thicknesses decrease, laser machined pore sizes decrease while permeability increases. This finding may have profound effects on future research directions.

5.5 Discussion of Micromolded Membrane Results

Permeability results for micromolded membranes were not obtained. Two explorations were initially thought. First, it was found that release of the PDMS over SU8 posts was difficult even with PEG coatings. Maximum aspect ratios of membrane/pores size were on the order of 3:1 due to the post release problem. Thicker membranes (higher aspect ratio) tend to have SU8 posts stuck inside the pore and block the mass flow. To verify that the posts were not intact within 3:1 membranes, an AFM was performed. It's shown in Figure 27. This indicates that at 3:1 aspect ratio, mold release was not an issue.

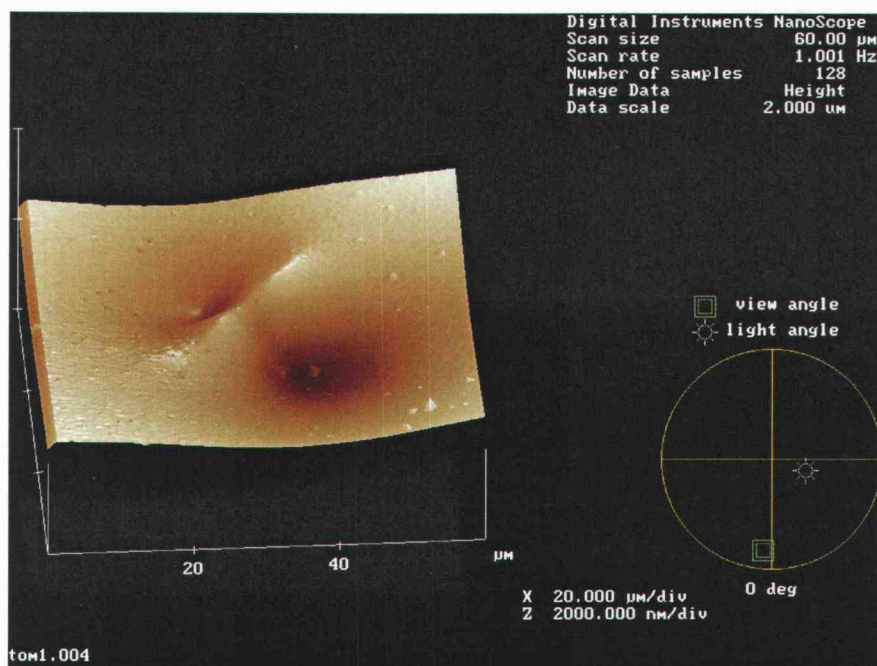


Figure 27: Front side of PDMS membrane pore

Second, as indicated in Figure 27, the pore seems to have collapsed. To investigate the shape of the pore, pictures were taken before and after the application of IPA. The PDMS was known to swell in the presence of isopropyl alcohol (IPA). We found out that the holes are grossly deformed before applying the IPA solution (See Figure 28). After IPA application, the membrane starts to expand and eventually the

sealed pore will be opened (See Figure 29 and Figure 30). In order to keep the holes from collapsing, it was found that IPA solution must be continually applied.

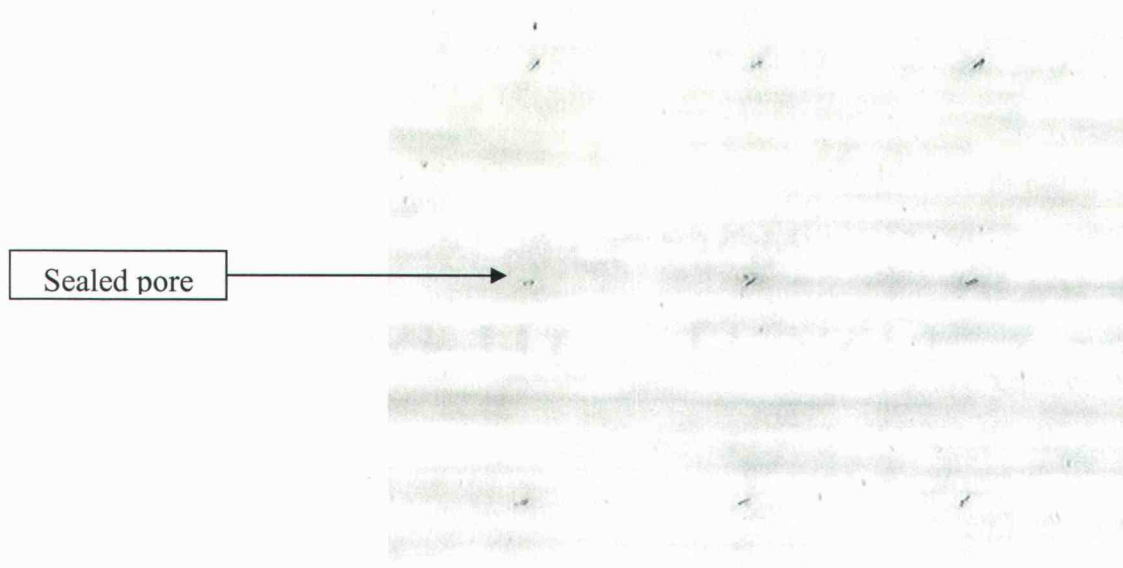


Figure 28: Sealed PDMS pores before application of IPA.

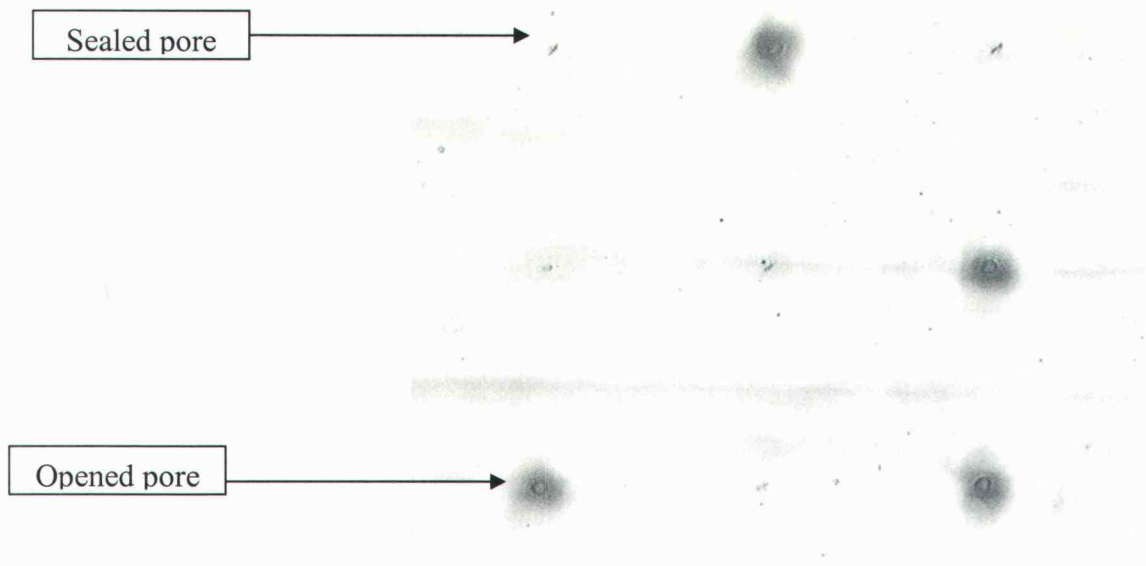


Figure 29: Portion of PDMS pores opened after few drops of IPA

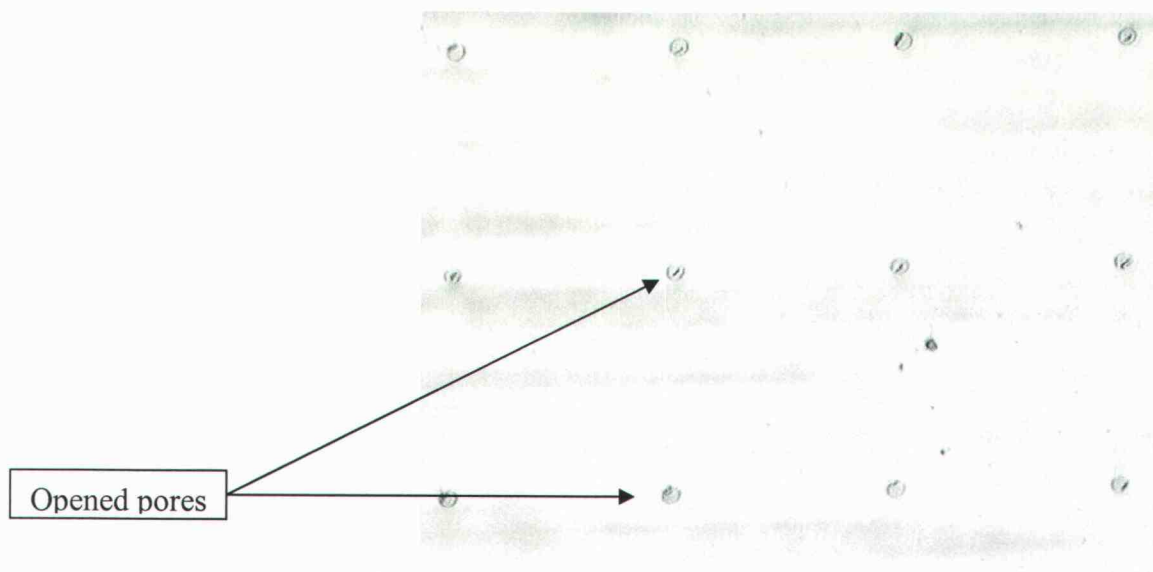


Figure 30: All PDMS pores opened after full application of IPA.

We successfully produced micromolded membranes with straight through pores (Appendix H). The membrane was verified under an optical microscope (Figure H-18 to Figure H-230) and an atomic force microscope (Figure 27). The thickness of the PDMS membrane thickness was $15\ \mu\text{m}$. Problems were incurred when the membranes were tested in the test loop. We are not able to get readings of the pressure drop since it is out of range for our digital manometer. We discover that the front side of the pore opening tends to deform once it is dried.

Using the AFM, the cross section of the pore was also measured. The vertical height differences of the two surface indents adjacent to the middle ridge are 956.56 and 540.87 nm, respectively (Figure 311 and Figure 322). From the pictures, we are able to confirm no posts are inside the pore and that the opening of the pore has been sealed.

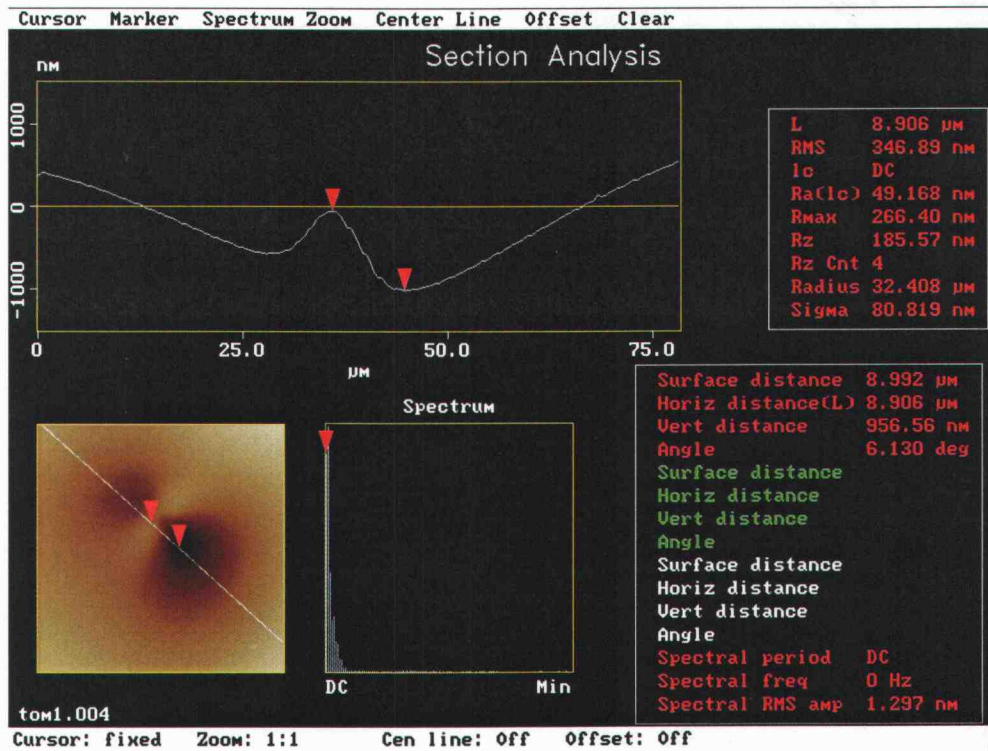


Figure 31: AFM picture of a pore A

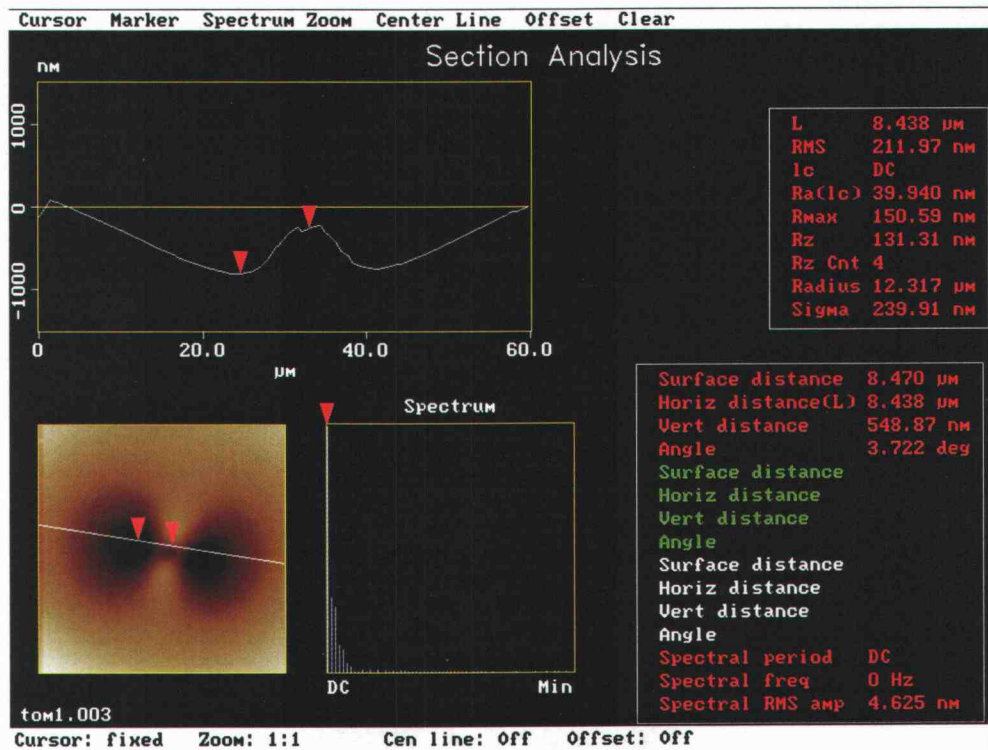


Figure 32: AFM picture of a pore B

To eliminate the collapsing of the PDMS, further investigations could be performed to investigate the effect of the elastic modulus of the PDMS on the deformation of the pores by changing the ratio of the crosslinker from 1:10 to 1:5 or less. In other words, this process of reducing the base oligomer will stiffen the membrane since the membrane is more crosslinked.

CHAPTER 6

CONCLUSION

In this thesis, a mass flux data baseline was developed regarding the permeabilities of various commercial and microengineered liquid-gas contactor membranes for absorption cycle heat pump applications. Laser-machined membranes showed over 30 times the permeability of conventional membranes with same sized pores. Further, laser-machined membranes maintained the lowest porosities indicating that these membranes may ultimately be stiffer. A trend in the laser-machined membrane data suggests that thinner membranes would lead to both higher permeabilities with smaller pore sizes which is good for minimizing liquid-gas breakthrough. These findings have interesting implications for the future design of microengineered contractor membranes.

Some commercial membranes were also found to have excellent permeability as well. In particular, woven membranes were found to have the largest overall permeabilities found within the study. It is anticipated that the stiffness and breakthrough pressure of woven membranes would be a problem for future contactor applications. Also, PES membranes were found to have similar permeabilities with laser machined membranes. Of all the non-engineered membranes in this study, the PES membranes were found to perform best (by more than 10 times). Reasons include that the pores of the PES membranes most closely emulate those of straight-through pores. Issues with the PES membranes are that they are highly porous and may not be able to provide the stiffnesses required to maintain the dimensions of adjacent microchannels.

Permeability results for micromolded membranes were not obtained due to the collapsing of elastomeric pores. Recommendations had been made by changing the ratio of the crosslinker from 1:10 to 1:5 or less. This would stiffen the membrane and prevent collapsing of the PDMS pores.

Future studies are encouraged to take advantage of straight through pores by evolving a membrane structure that permits smaller laser-machined pores into a stiff, micromolded membrane structure. Future studies will need to take into consideration the breakthrough pressures of microengineered contactor membranes by considering the hydrophobicity and pore size of membrane materials.

References

Champagne Peter R., Bergles Arthur E.,

“Development and Testing of a Novel Variable-Roughness Technique to Enhance, on Demand, Heat Transfer in a Single-Phase Heat Exchanger”, vol. 8, pp. 341-352, 2001

Davis, S.C.,

Transportation Energy Data Book, Oak Ridge National Laboratory, Oak Ridge, Tennessee

Drost, M.K.,

“Mesoscopic Heat-Actuated Heat Pump Development”, *Proceedings of the ASME Advanced Energy Systems*, AES-vol 39, pp. 9-19, 1999

Duffy, D.C., Jackman, R.J., Vaeth, K.M., Jensen, K.F. and Whitesides, G.W.

“Patterning Electroluminescent Materials with Feature Sizes as Small as 5 μm Using Elastomeric Membranes as Masks for Dry Lift-off”, *Adv. Materials*, vol. 11 (7), pp. 546-552, 1999

Ho W. S. Winston, Kamalesh K. Sirkar,

“Membrane Handbook”, *Van Nostrand Reinhold*, 1992

Iversen S. B., Bhatia V.K., Dam-Johansen K., Jonsson G.,

“Characterization of Microporous Membranes for Use in Membrane Contactors”, *Journal of Membrane Science*, Vol. 130, pp. 205-217, 1997

Jackman, R.J., Duffy, D.C., Chernavskaya, O and Whitesides, G.W.,

“Using Elastomeric Membranes as Dry Resists and for Dry Lift-Off”, *Langmuir*, 15, pp. 2973-2984

Kim Kyu-Jin, Paul V. Stevens, Anthony G. Fane,

“Porosity Dependence of Pore Entry Shape in Track-Etched Membranes by Image Analysis”, *Journal of Membrane Science*, vol. 93, pp. 79-90, 1994

Kikuchi, Kaoru, Green, Peter W., Maeda, Ryutaro,

“Micromachining of Silicon Wafer and Pyrex Glass with Excimer Laser”, *Kikai Gijutsu Kenkyusho Shoho/Journal of Mechanical Engineering Laboratory*, v. 51, n. 2, Mar 1997

Kuhn, Kelin J.,

“Laser Engineering”, Prentice-Hall, Inc, 1998

TeGrotenhuis W.E., Cameron R.J., Viswanathan V.V., Wegeng R.S.,

“Solvent Extraction and Gas Absorption Using Microchannel Contactors”, Pacific Northwest National Laboratory, PO Box 999, Richland, WA 99352 USA

McDonald J. Copper, Whitesides George M.,

“Poly (dimethylsiloxane) as a Material for Fabricating Microfluidic Devices”, *Accounts of Chemical Research*, vol. 35, no. 7, 2002

Mulder Marcel

“Basic Principles of Membrane Technology”, *Kluwer Academic Publishers*, 1990

Nakao Shin-ichi

“Review: Determination of Pore Size Distribution 3. Filtration Membranes”, *Journal of Membrane Science*, vol. 96, pp. 131-165, 1994

Palacio L., Pradanos P., Calvo J.I., Hernandez A.,

“Porosity Measurements by a Gas Penetration Method and Other Techniques Applied to Membrane characterization”, *Thin Solid Films*, vol. 348, pp. 22-29, 1999

Plessis J.P.,

“Geometrical Models for Porous Membrane Morphologies”, *Wat. Sci. Tech.*, vol. 25, no. 10, pp. 363-372, 1992

Salmas Constantinos E., Androutsopoulos George P.,

“A Novel Pore Structure Tortuosity Concept Based on Nitrogen Sorption Hysteresis Data”, *Ind. Eng. Chem. Res.*, vol. 40, pp. 721-730, 2001

Saripalli K. Prasad, Serne R. Jeffery, Meyer Philip D., McGrail B. Peter,

“Prediction of Diffusion Coefficients in Porous Media Using Tortuosity Factors Based on Interfacial Areas”, *Ground Water*, vol. 40, no. 4, pp. 346-352, Jul-Aug 2002

Shelekhin A. B., Dixon A.G, Ma Y.H.,

“Adsorption, Diffusion and Permeation of Gases in Microporous Membranes. III.”, *Journal of Membrane Science*, vol. 83, pp. 181-198, 1993

White, Frank M.,

“Fluid Mechanics”, McGraw-Hill Book Co., 1994

Zhao J.X., Juettner, B., Menschig, A.,

“Micromachining with ultrashort laser pulses”, *Proceedings of SPIE – The International Society for Optical Engineering*, vol. 3618, pp. 114-121, 1999

Bibliography

Beuscher Uwe, Gooding Charles H.,

“The Permeation of Binary Gas Mixtures Through Support Structures of Composite Membranes”, *Journal of Membrane Science*, vol. 150, pp. 57-73, 1998

Bodzed Michal, Konieczny Krystyna,

“The Influence of Molecular Mass of Poly (Vinyl Chloride) on the Structure and Transport Characteristics of Ultrafiltration Membranes”, *Journal of Membrane Science*, vol. 61, pp. 131-156, 1991

Childs William R., Nuzzo Ralph G.,

“Decal Transfer Microlithography: A New Soft-Lithographic Patterning Method”, *Journal of American Chemical Society*, vol. 124, pp. 13583-13596, 2002

Duchet J., Demoustier-Champagne S.,

“Study of Polystyrene Microstructures and Nanostructures Synthesised in Particle Track-Etched Membranes Used as Temples”, *Polymer*, v. 41, pp. 1-8, 2000

Kaneko Katsumi,

“Determination of Pore Size and Pore Size Distribution 1. Adsorbents and Catalysts”, *Journal of Membrane Science*, vol. 96, pp. 59-89, 1994

Kokubo Ken-ichi, Sakai Kiyotaka,

“Evaluation of Dialysis Membranes Using a Tortuous Pore Model”, *AIChE Journal*, vol. 44, no. 12, pp. 2607-2619, Dec 1998

Kreulen H., Smolders C.A., Versteeg G.F., Van Swaaij W.P.M.,

“Determination of Mass Transfer Rates in Wetted and Non-Wetted Microporous Membranes”, *Chemical Engineering Science*, vol. 48, no. 11, pp. 2093-2102, 1993

MacDonald Rosemary A.,

“Modelling Macromolecular Diffusion Through a Porous Medium”, *Journal Membrane Science*, vol. 68, pp. 93-106, 1992

Magistris A., Mustarelli P., Parazzoli F., Quartarone E., Piaggio P., Bottino A.,

“Structure, Porosity and Conductivity of PVdF Films for Polymer Electrolytes”, *Journal of Power Sources*, vol. 97-98, pp. 657-660, 2001

Maskell W.C.,

“Tortuosity Factor in Non-Homogeneous Membrane”, *Ber. Bunsenges. Phys. Chem.*, no. 5, pp. 680-683, 1993

Montassier N., Dupin L., Boulaud D.,

“Experimental Study on the Collection Efficiency of Membrane Filters”, *Journal Aerosol Science*, vol. 27, suppl. 1, pp. S637-S638, 1996

Sakai, K.,

“Determination of Pore Size and Pore Size Distribution 2. Dialysis Membranes”, *Journal of Membrane Science*, vol. 96, pp. 91-130, 1994

Quartarone E., Mustarelli P., Magistris A.,

“Transport Properties of Porous PVDF Membranes”, *Journal of Phys. Chem. B*, vol. 106, pp. 10828-10833, 2002

Tessendorf Stefan, Gani Rafiqul, Michelsen Michael L.,

“Modeling, Simulation and Optimization of Membrane-Based Gas Separation Systems”, *Chemical Engineering Science*, vol. 54, pp. 943-955, 1999

Wolf Jeffery R., Strieder William,

“Surface and Void Tortuosities for a Random Fiber Bed: Overlapping, Parallel Cylinders of Several Radii”, *Journal of Membrane Science*, vol. 49, pp. 103-115, 1990

Zeman Leos,

“Characterization of Microfiltration Membranes by Image Analysis of Electron Micrographs. Part II. Functional and Morphological Parameters”, *Journal of Membrane Science*, vol. 71, pp. 233-246, 1992

Appendices

Appendix A

Table 1 shows a list of the membranes selected for establishing the membrane mass flux baseline.

Each table provides a micrograph illustrating the morphology of each membrane.

Table A-1: Specifications for nylon membranes included in the mass flux baseline.

Material	Pore size	Thickdiness		Weight (g)	Size (mm OD)	Density (g/cm ³)	M. Density (g/cm ³)	Company	Part No
	Micron	Micron	Mil						
Nylon	10	88.90	3.50	0.0026	square	N/A	1.14	Osmonics	R99SP320FX
Nylon	5	99.06	3.90	0.0243	25	0.49973303	1.14	Osmonics	R50SP02500
Nylon	1.2	106.68	4.20	0.0643	25	1.22788606	1.14	Osmonics	R12SP02500
Nylon	1	106.68	4.20	0.1014	47	0.54785969	1.14	Pall (Gelman)	66509
Nylon	1.2	101.60	4.00	0.0260	25	0.52132643	1.14	ADVANTEC MFS	N120A025A

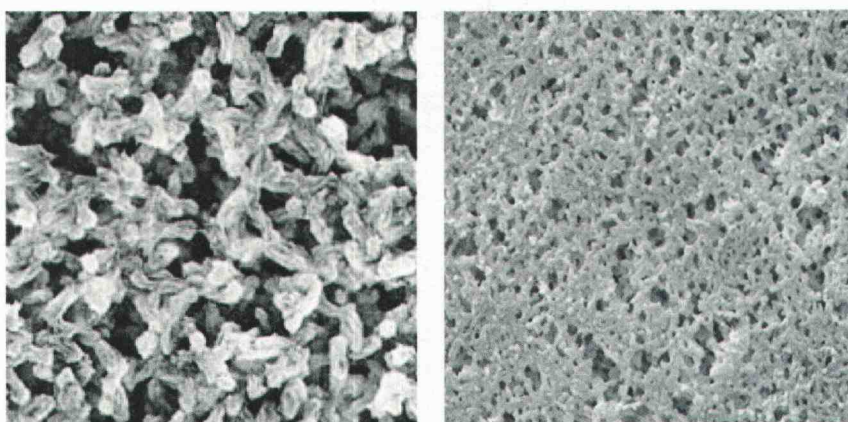


Figure A-1: Micrographs of a nylon membrane.

Table A-2: Specifications for polyethersulfone membranes included in the mass flux baseline.

Material	Pore size	Thickness		Weight (g)	Size (mm OD)	Density (g/cm ³)	M. Density (g/cm ³)	Company	Part No
	Micron	Micron	Mil						
Polyethersulfone - PES	5	106.68	4.20	0.0113	25	0.21579	1.37000	Osmonics	S50SP02500
Polyethersulfone - PES	1.2	114.30	4.50	0.0115	25	0.20497	1.37000	Osmonics	S12SP02500
Polyethersulfone - PES	0.8	129.54	5.10	0.0125	25	0.19658	1.37000	Osmonics	S08SP02500

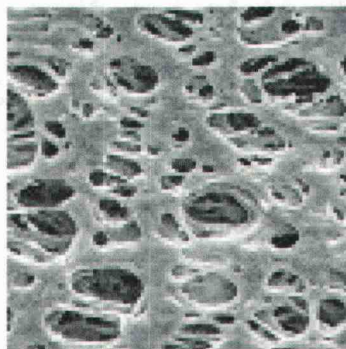
**Figure A-2:** Micrograph of a polyethersulfone membrane.

Table A-3: Specifications for PVC membranes included in the mass flux baseline.

Material	Pore size	Thickness		Weight (g)	Size (mm OD)	Density (g/cm ³)	M. Density (g/cm ³)	Company	Part No
	Micron	Micron	Mil						
Polyvinyl Chloride – PVC	5	55.88	2.20	0.0075	25	0.27342	1.40000	Pall (Gelman)	66466
Polyvinyl Chloride – PVC	5	152.4	6.00	0.0078	25	0.10427	1.40000	Millipore	PVC502500

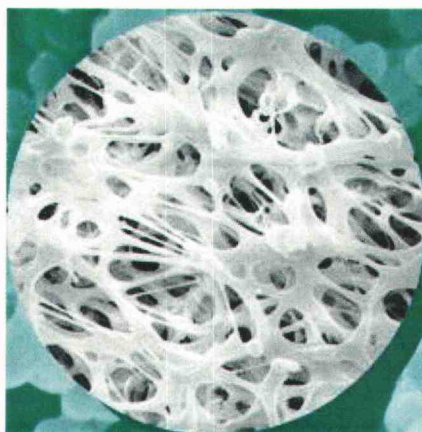
**Figure A-3:** Micrograph of a PVC membrane.

Table A-4: Specifications for Polypropylene membranes included in the mass flux baseline.

Material	Pore size	Thickness		Weight (g)	Size (mm OD)	Density (g/cm ³)	M. Density (g/cm ³)	Company	Part No
		Micron	Mil						
Polypropylene	10	116.84	4.60	0.0234	25	0.40799	0.91000	Millipore	AN1H02500
Polypropylene	10	88.90	3.50	0.0947	47	0.61399	0.91000	Pall (Gelman)	61757
Polypropylene	5	101.60	4.00	0.0257	25	0.51531	0.91000	Millipore	AN5002500
Polypropylene	2.5	121.92	4.80	0.0412	25	0.68842	0.91000	Millipore	AN2502500
Polypropylene	1.2	116.84	4.60	0.0412	25	0.71835	0.91000	Millipore	AN1202500

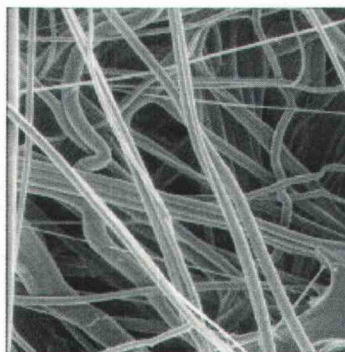
**Figure A-4:** Micrograph of a polypropylene membrane.

Table A-5: Specifications for polyvinylidene fluoride membranes included in the mass flux baseline.

Material	Pore size	Thickness		Weight (g)	Size (mm OD)	Density (g/cm ³)	M. Density (g/cm ³)	Company	Part No
		Micron	Mil						
Polyvinylidene Fluoride	5	109.22	4.30	0.0347	25	0.64723	1.78000	Millipore	SVLP02500

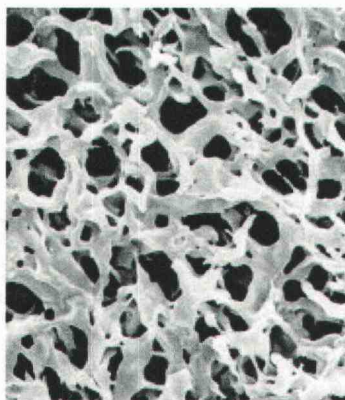
**Figure A-5:** Micrograph of a polyvinylidene fluoride membrane.

Table A-6: Specifications for PTFE membranes included in the mass flux baseline.

Material	Pore size	Thickness		Weight (g)	Size (mm OD)	Density (g/cm ³)	M. Density (g/cm ³)	Company	Part No
	Micron	Micron	Mil						
Polytetrafluoroethylene PTFE	10	132.08	5.20	0.0823	25	1.26938	2.19000	Osmonics	Z99WP02550
Polytetrafluoroethylene PTFE	10	93.98	3.70	0.0432	25	0.93644	2.19000	Millipore (Mitex)	LCWP02500
Polytetrafluoroethylene PTFE	5	162.56	6.40	0.0828	25	1.03764	2.19000	Osmonics	Z50WP02550
Polytetrafluoroethylene PTFE	5	157.48	6.20	0.0825	25	1.06723	2.19000	Millipore (Mitex)	LSWP02500
Polytetrafluoroethylene PTFE	5	134.62	5.30	0.1751	37	1.20972	2.19000	Pall (Gelman)	P4PH037
Polytetrafluoroethylene PTFE	3	127	5.00	0.0219	25	0.35129	2.19000	Millipore (Fluoropore)	FSLW02500

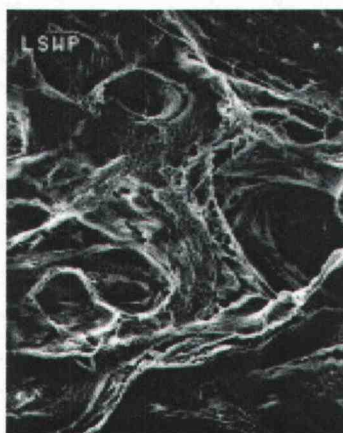
**Figure A-6:** Micrograph of a PTFE membrane.

Table A-7: Specifications for MCE membranes included in the mass flux baseline.

Material	Pore size	Thickness		Weight (g)	Size (mm OD)	Company	Note	Part No
	Micron	Micron	Mil					
Mixed Cellulose Ester (MCE)	8	135	5.31	0.0579	47	Millipore	Hydrophilic	SCWP04700
Mixed Cellulose Ester (MCE)	5	160	6.30	0.0185	25	ADVANTEC MFS		A500A025A
Mixed Cellulose Ester (MCE)	5	135	5.31	0.0682	47	Millipore	Hydrophilic	SMWP04700
Mixed Cellulose Ester (MCE)	3	150	5.91	0.0799	47	Millipore	Hydrophilic	SSWP04700

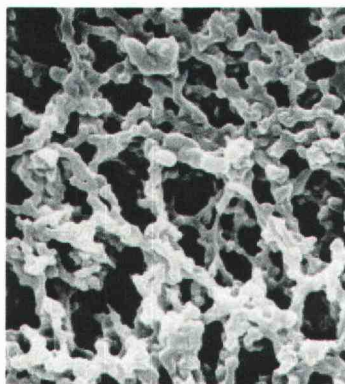
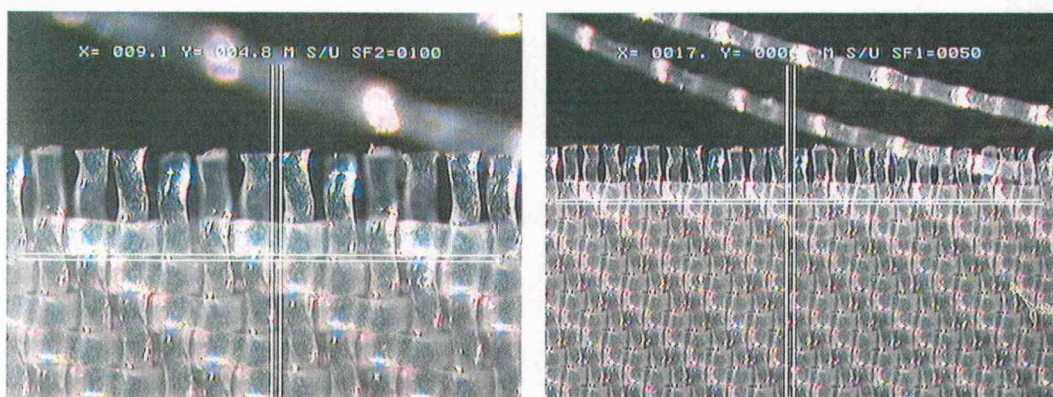
**Figure A-7:** Micrograph of a MCE membrane.

Table A-8: Specifications for polyamide woven membranes included in the mass flux baseline.

Material	Pore size	Open Area	Thickness		Size (mm OD)	Company	Part No
	Micron		Micron	Mil			
Polyamide - PA	7	2%	78	3.07	TBD	SaatiTech	PA 7/2

**Figure A-8:** Micrograph of a polyamide woven membrane.

Appendix B

The following are the procedures for focusing the laser to substrate and Figure B-1 shows the layout of the laser micromachining bench

1. Measure the thickness of the material
2. Put the material on the stage and make sure it is flat
3. Turn on the laser machine (do not press N on the keyboard)
4. Turn on the power supply and gradually increase the power to 18
5. Focus on the surface using the lens micrometer and then back off half of a turn
6. Press N at the keyboard and then press any key to start the calibrating process
7. Initial focusing process
 - a. Run a four dot matrix program with 1000 micron spacing
 - b. Raise stage height by 1 division and shift the X-axis by 10 minor divisions
 - c. Go back to step b. and repeat 8 times
 - d. Remove the material from the stage and carry to the microscope
 - e. Inspect the laser markings, choosing the group with the best focus.
 - f. Note the sequence of the group counting from the left.
 - g. Lower the stage to the level at which the selected group was cut.
8. Fine focusing process
 - a. Lower the stage 0.4 division
 - b. Raise stage height by 0.1 division and shift the X-axis by 10 minor divisions
 - c. Go back to b. and repeat for 8 times
 - d. Remove the material from the stage and carry to the microscope
 - e. Inspect the laser markings, choosing the group with the best focus.
 - f. Note the sequence of the group counting from the left.
 - g. Lower the stage to the level at which the selected group was cut.
9. Get the correct focus then move the stage up half the thickness of material
10. Done

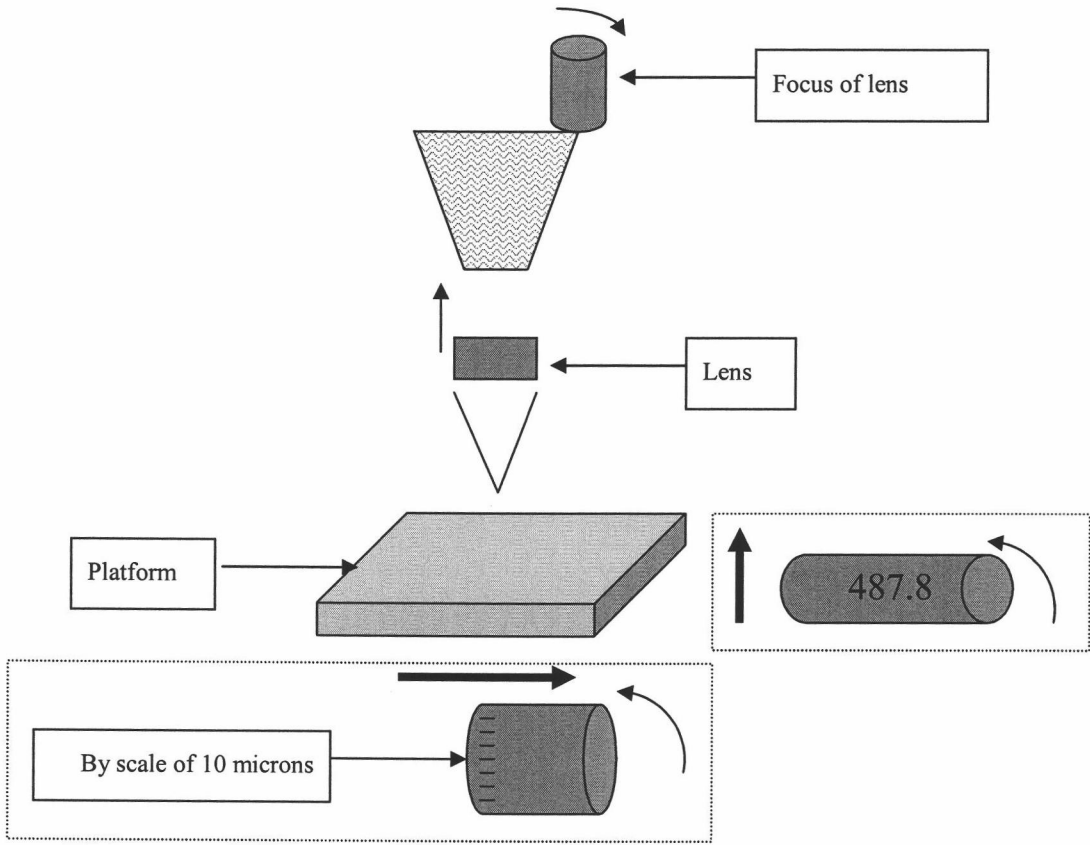


Figure B-1: Layout of the laser micromachining bench.

Appendix C

Five areas of the work piece had been chosen to verify the flatness. The machine drilled series of holes at each area then the size of the hole were measured. Three individual tests had been performed and documented. Figure C-1, C-2, an C-3 show the result verified by the optical microscope.

Table C-1: Dimension of the hole under optical microscope

Upper left (A) (microns)		Upper right (B) (microns)	
1	241.6	1	209.1
2	246.7	2	215.2
3	225.4	3	210.2
Avg.	237.9	Avg.	211.5

Center (C) (microns)	
1	217.3
2	224.4
3	227.4
Avg.	223.03

Lower left (D) (microns)		Lower right (E) (microns)	
1	237.6	1	212.2
2	239.6	2	236.5
3	236.5	3	220.3
Avg.	237.9	Avg.	223

Average =	226.7	um
Maximum =	237.9	um
Minimum =	211.5	um
Max. Variance =	26.4	um
Standard Deviation =	11.28	um
Deviation Percentage =	4.98%	

Test 1 (result)

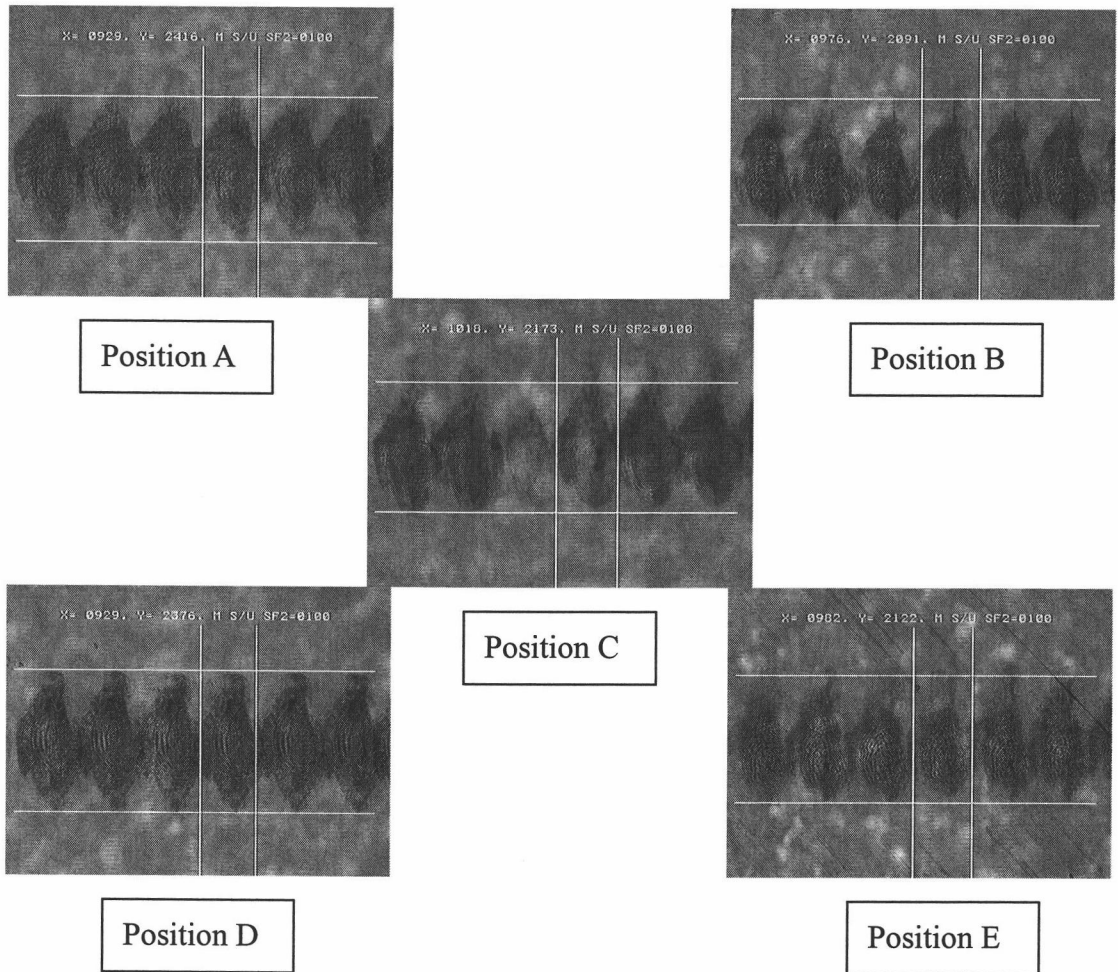


Figure C-1: First test results

Test 2 (result)

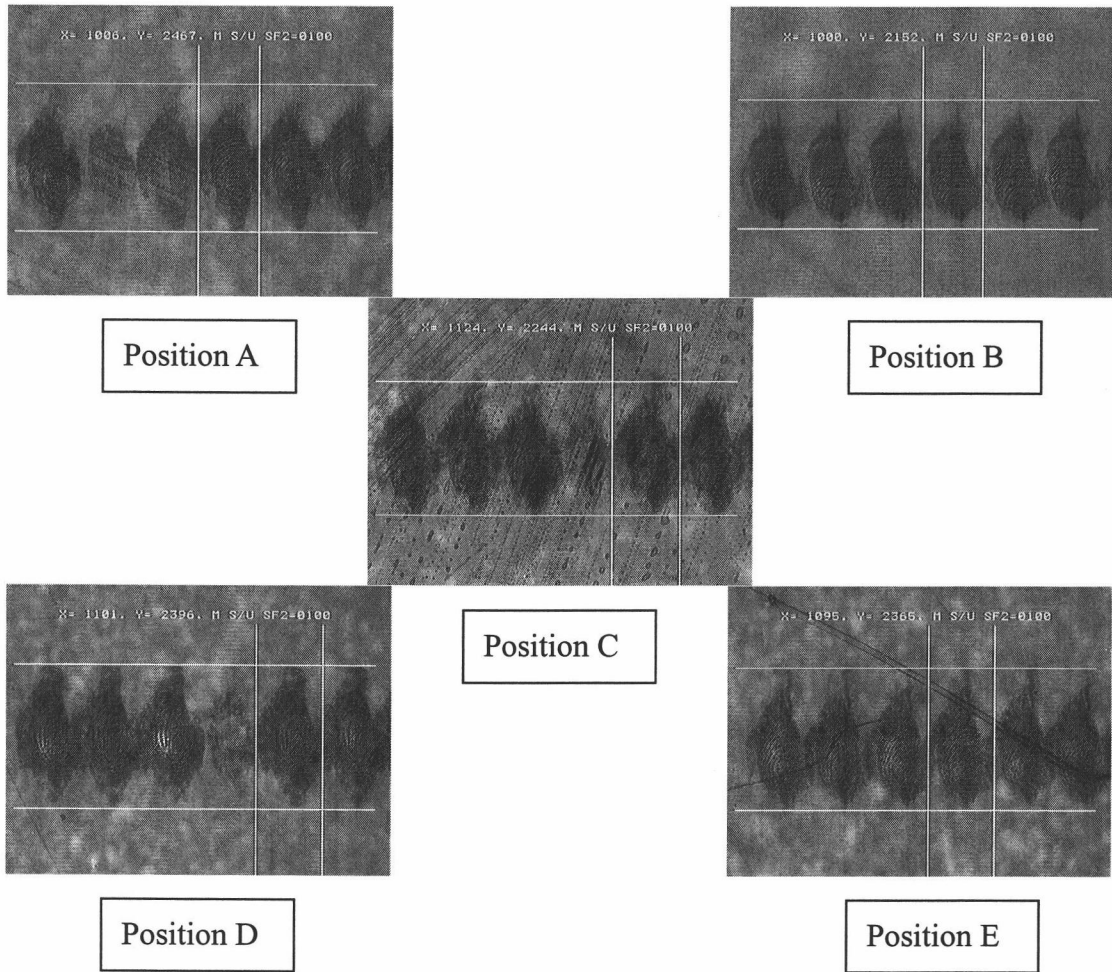


Figure C-2: Second test results

Test 3 (result)

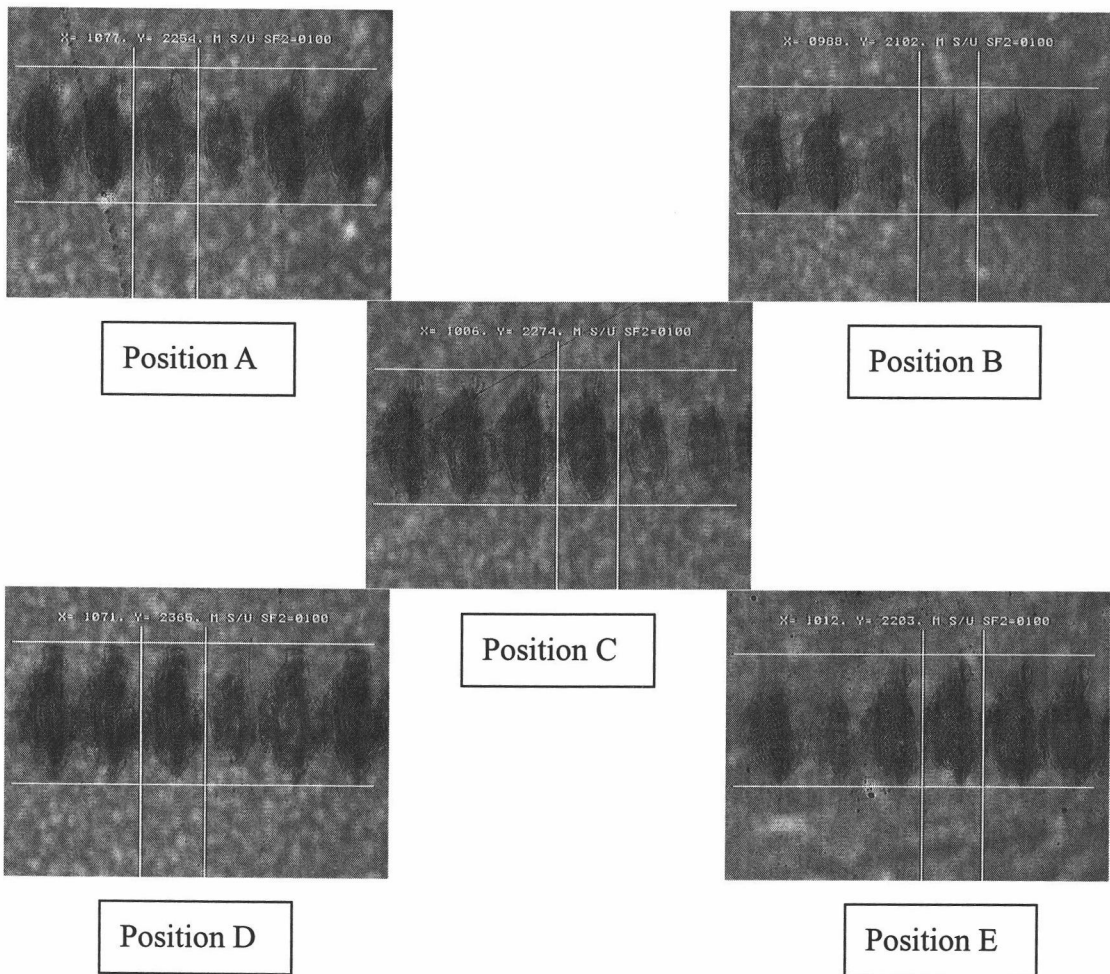


Figure C-3: Third test results

Appendix D

The test fixture and test procedure were referenced from PNNL's design (See Appendix E).

Initial Check

1. Turn the valve under the pressure gauge to horizontal position. (Note: this will close the valve in order to protect the instruments)

Fixture and sample setup

1. Cut the sample to appropriate size then use tweezers to set in the middle of fixture.
2. Put the Viton gasket above the sample and align with 8 screw holes.
3. Put the stiffener above the gasket and screw tightly until complete sealed
4. Cover the upper lid and screw tightly until complete sealed
5. Attach the upper lid with out-line flow tube to mass flowmeter.
6. Attach the lower part on the side of the fixture to difference pressure instrument's in-let. Attach the upper part on the side of the fixture to difference pressure instrument's out-let. (Note: Reverse setup will cause instrument damage!!)

Nitrogen flow setup

1. Adjust the needle valve to 0-10 position.
2. Counterclockwise turn on the nitrogen gas tank.
3. Adjust the knob until gauge readout as 400 cc/min.
4. Check the first pressure gauge and see if it is below 8 psi. If it is below 8 psi then move on to next step. If it is above 8 psi then go back to 3. and adjust the knob to appropriate flowrate. (Note: most of the instrument can not with hold above 10 psi of pressure)
5. Attach the nitrogen flow tube to the bottom of the fixture.
6. Setup complete

Appendix E

Air permeability test from PNNL

The air permeability test is intended to measure the permeability of the membranes. This is a measurement of the flow resistance of the membrane to gas or vapor flow. The configuration for this test is shown in Figure 1. In this test, a gas cylinder is used to supply the gas to the contactor test fixture. Compressed nitrogen or air can be used.

The gas cylinder is connected through a regulator to a fitting on a flow control valve which is attached to the test fixture. The gas goes through the sample, out the fitting above the sample, and through a flow meter before being exhausted to the ambient. A differential pressure measurement is set up between the second fitting below the sample and the gas stream before the flow meter.

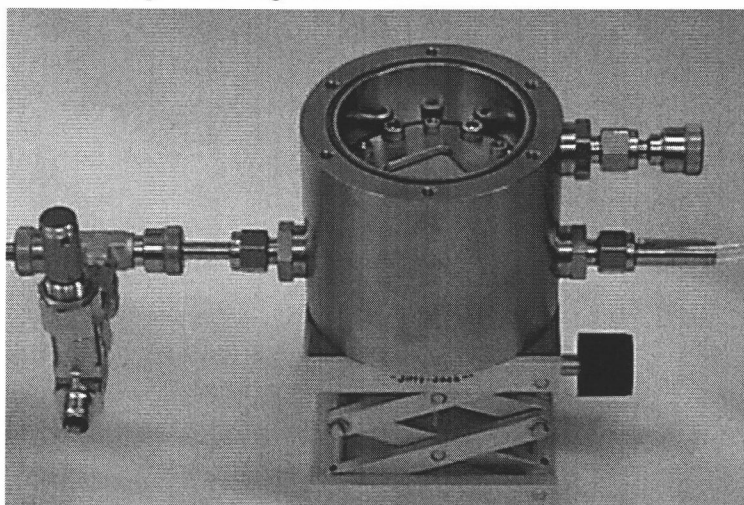


Figure E-1: Facility Configuration for Air Permeability Test

The test procedure is:

1. Install the membrane sample in the test fixture.
2. Place the lid on the test fixture
3. Set the regulator on the gas cylinder to approximately 2 psig.
4. Open the flow control valve until there is a measurable reading on the flow meter. Record the flow rate and the differential pressure.
5. Repeat this measurement at several (10-15) flow rates, up to the limit of the differential pressure transducer or the maximum flow rate supported by the flow meter. Steps in differential pressure of 1 to 2 inches are acceptable.
6. When the testing is complete, close the gas cylinder valve and the flow control valve. Once the differential pressure indicates no pressure difference, the fixture can be opened and the sample removed.

Appendix F

Repeatability tests had been performed before measurements been taken. A new test sample was cut from the Sattitech 7 μm woven membrane each time and measured its permeability then compared with previous results. The error rate was less than 7%. The #1 and #2 tests were performed during Mar-May 2002 and the #3 and #4 tests were performed during Nov 2003.

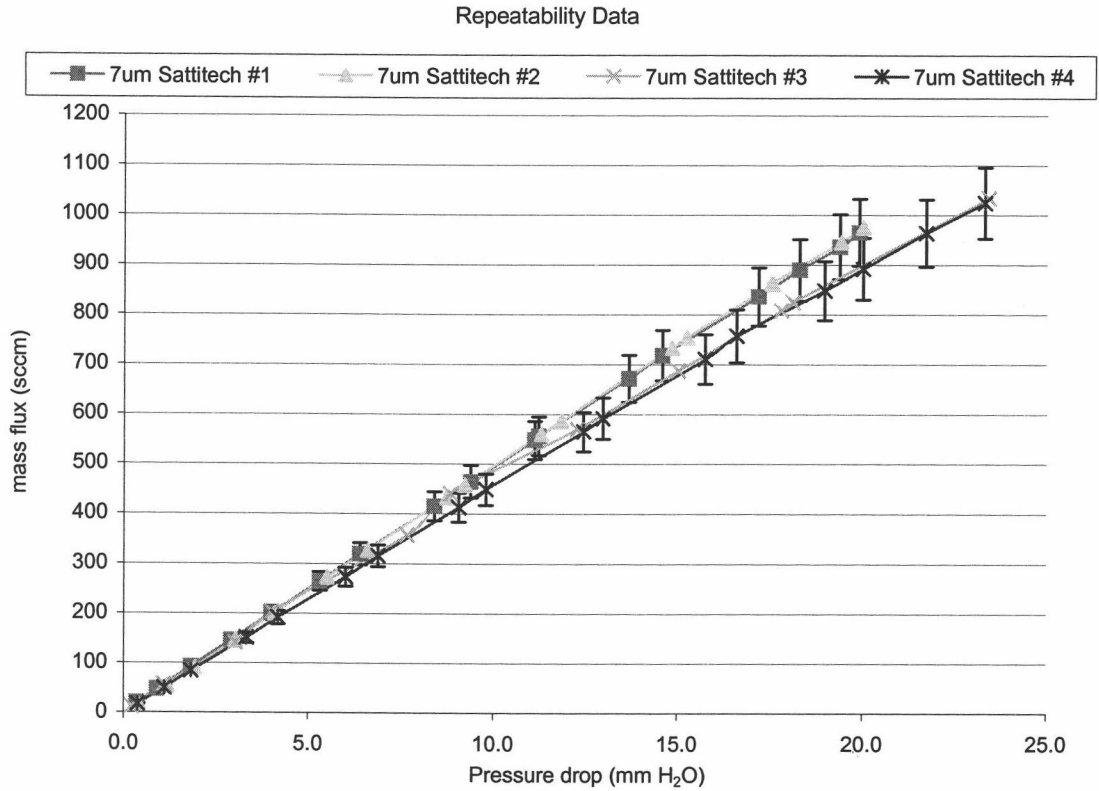


Figure F-1: Repeatability data

Appendix G

The laser micromachined membrane were taken to optical microscope and randomly measured 30 different pore dimensions and documented. From the 30 data points, standard deviation were calculated.

For example, here is the test result from the ESI membrane:

Pore	x	y	
1	5.8	4.0	
2	5.8	4.4	
3	5.3	5.6	
4	6.0	6.8	
5	5.5	4.6	
6	4.8	6.6	
7	7.0	4.6	
8	10.3	9.8	
9	5.6	4.0	
10	5.4	4.6	
11	5.0	4.6	
12	5.0	4.8	
13	4.7	4.8	
15	5.0	4.0	
16	5.5	4.8	
17	4.6	5.8	
18	4.6	5.6	
19	4.3	4.2	
20	4.4	4.0	
21	4.1	3.8	
22	4.1	4.0	
23	4.2	4.0	
24	4.1	4.4	
25	4.0	4.2	
26	4.1	4.0	
27	4.1	3.6	
28	4.7	4.6	
29	4.0	4.2	
30	3.0	3.6	
Average	4.8	4.6	4.72
STDEV	1.3	1.3	1.28

The result shows the ESI membrane had average pore size of $4.72 \pm 1.28 \mu\text{m}$

Appendix H

Two micromolded membranes with straight through pores were successfully produced and verified under optical microscope (Figure H-1 and Figure H-2).

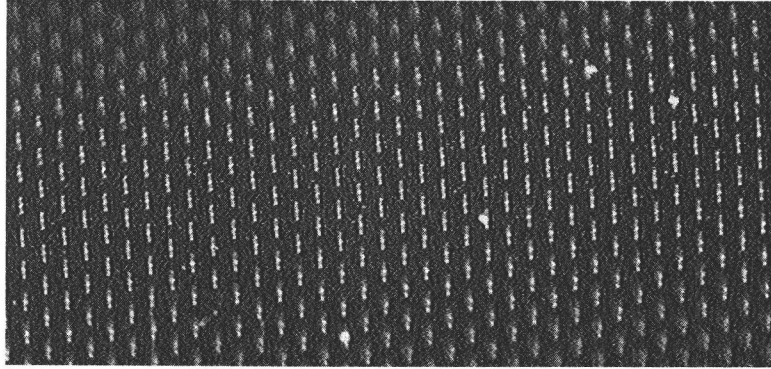


Figure H-1: Picture of $5\mu\text{m}$ diameter posts with height of $65\mu\text{m}$ (1:13 aspect ratio) on the silicon wafer

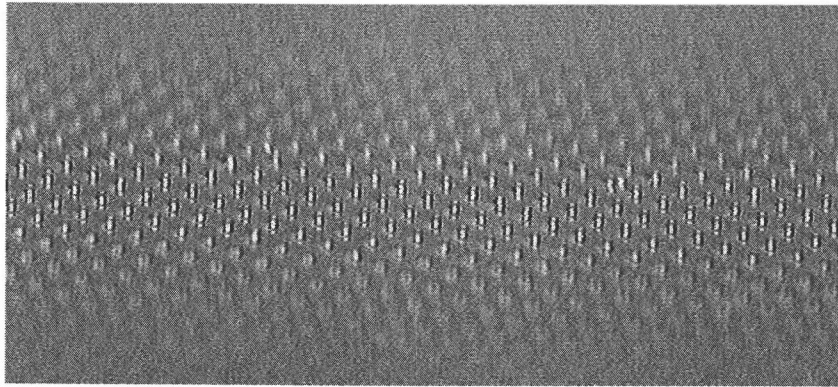


Figure H-2: PDMS spincoated onto SU8 micromold

H.1 SU8 Posts

Results show $5\mu\text{m}$ posts standing in various heights on silicon substrate. The highest aspect ratio achieved was 1:13 ($5\mu\text{m} : 60\mu\text{m}$). H-3, H-4, and H-5 are the SEM pictures showing SU8 posts on silicon substrate.

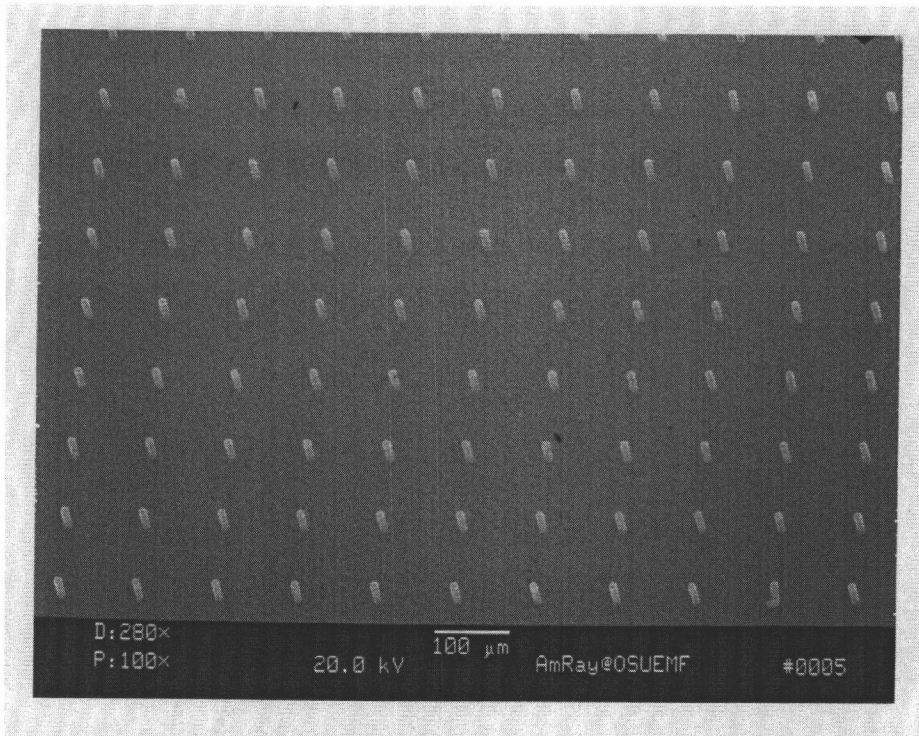


Figure H-3: SU8 post array (100X)

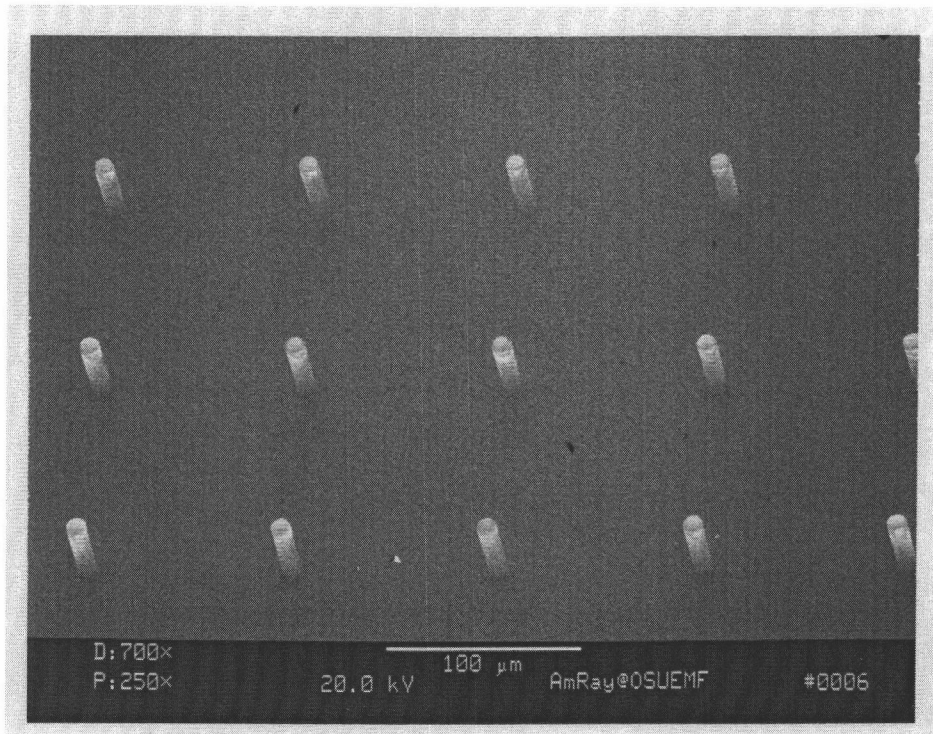


Figure H-4: SU8 post array (250X)

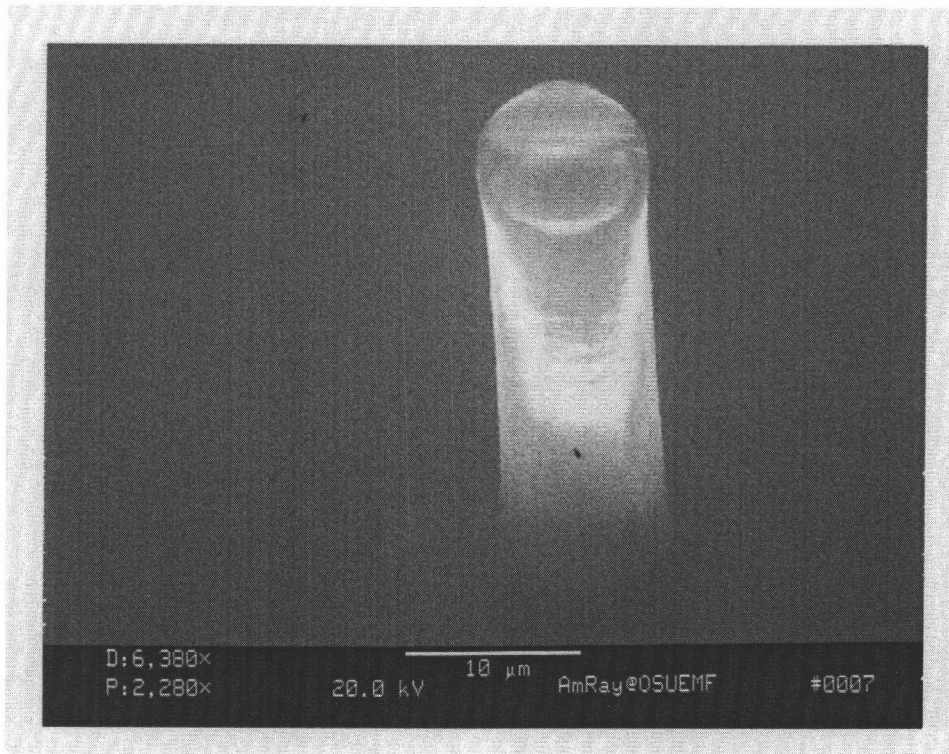


Figure H-5: SU8 post (2280X)

The SU8 was first spincoated onto the silicon substrate then proceed with photolithography process. Thus the spin speed controls the height of the SU8 post. The relationship between spin speed and SU8 height are plotted below on Figure H-6 and value listed at Table H-1.

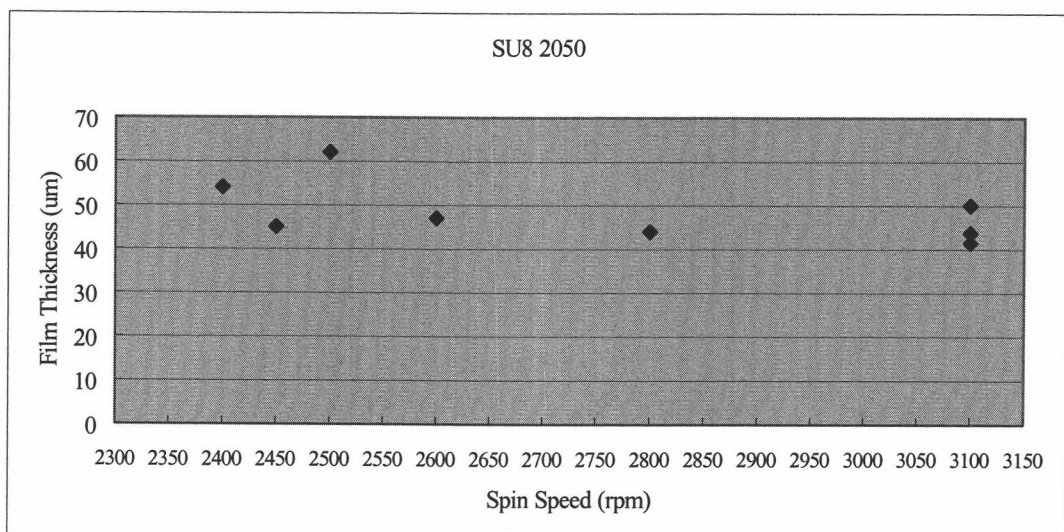


Figure H-6: Results from experiment

Table H-1: Experiment data

Experiment	#1	#2	#3	#4	#5	#6	#7	#8
Film Thickness (um)	2500	2600	2400	2450	3100	3100	3100	2800
Spin Speed (rpm)	62	47	54	45	43.7	50	41.4	44

H.2 PDMS

The PDMS was first spincoated onto the silicon substrate then cured. Thus the spin speed controls the thickness of the PDMS membrane. The relationship between spin speed and PDMS thickness are plotted below on Figure H-7 and value listed at Table H-2.

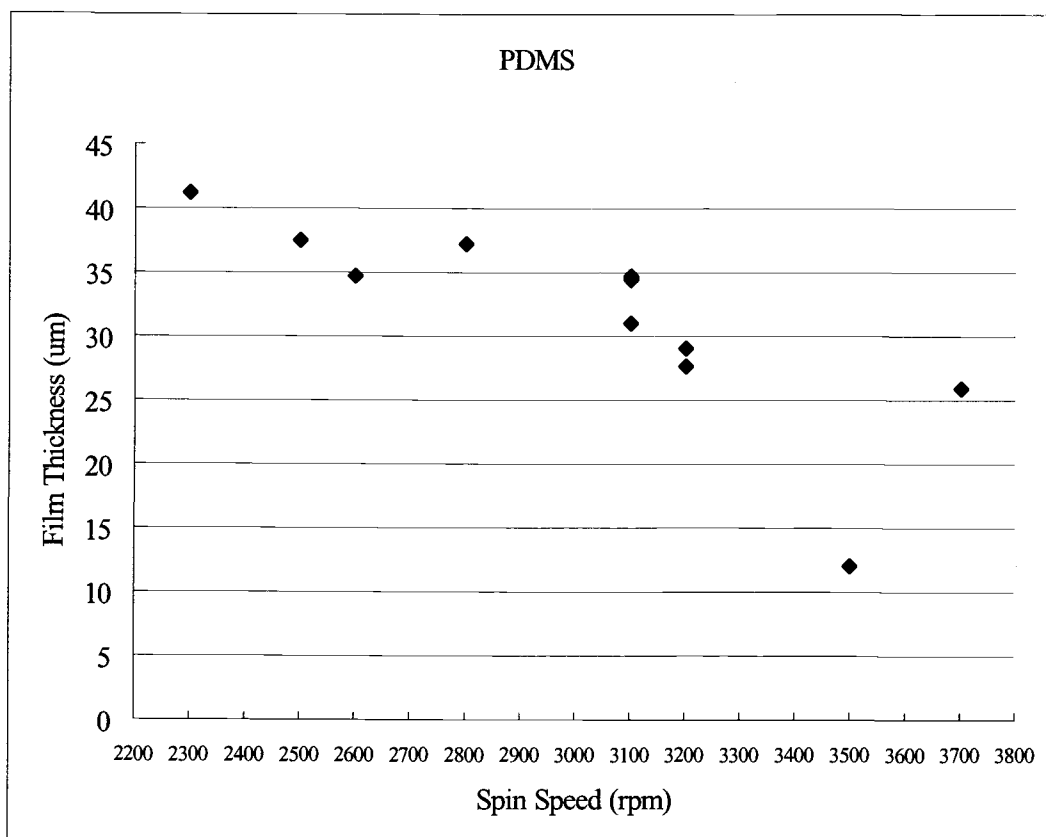


Figure H-7: PDMS thickness experiment results

Table H-2: PDMS experiments result

Film Thickness (um)	Spin Speed (rpm)
12.0	3500
25.9	3700
27.6	3200
29.0	3200
34.4	3100
34.5	3100
31.0	3100
34.7	3100
37.2	2800
37.5	2500
41.2	2300
4.7	2600

H.3 Sacrificial Layer

The result after coating sacrificial layer (PEG) is shown on H-8, H-9, H-10, and H-11.

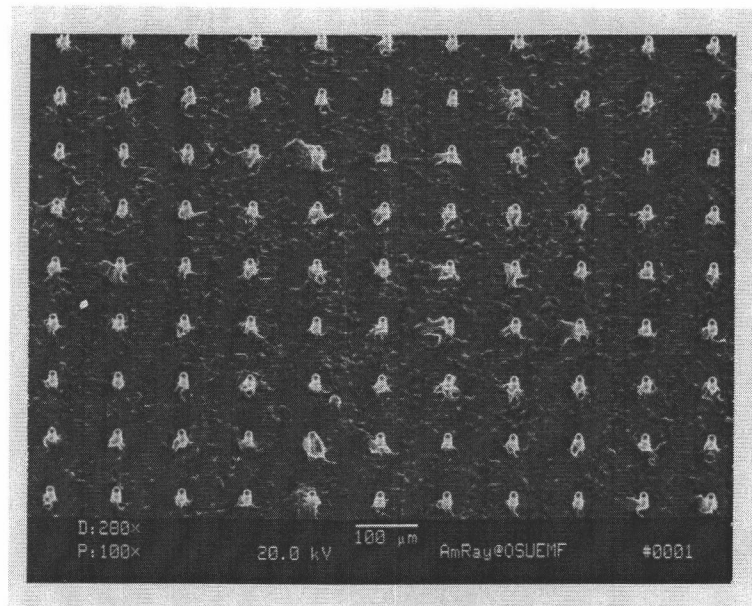


Figure H-8: SU8 post arrays coated with PEG (100X)

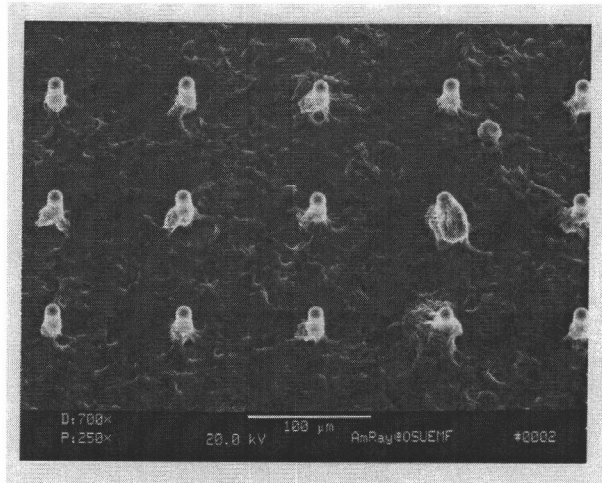


Figure H-9: SU8 post arrays coated with PEG (250X)

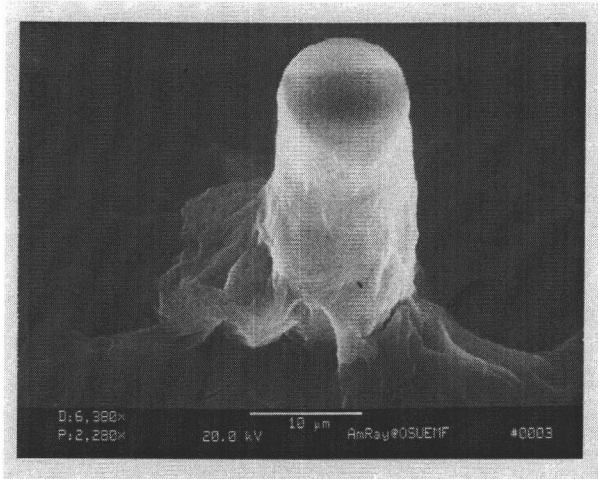


Figure H-10: SU8 post coated with PEG (2280X)

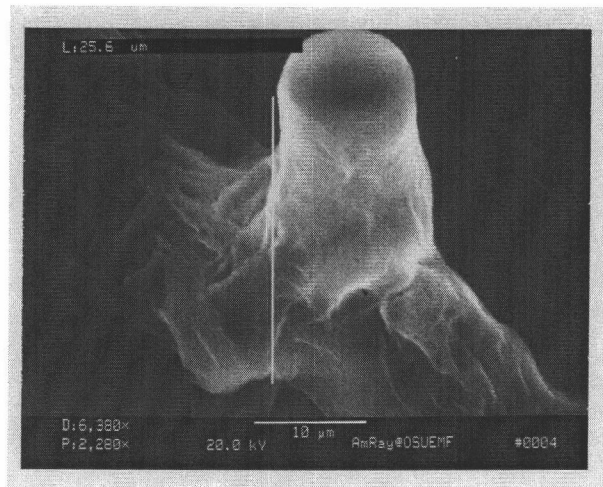


Figure H-11: SU8 post coated with PEG (2280X)